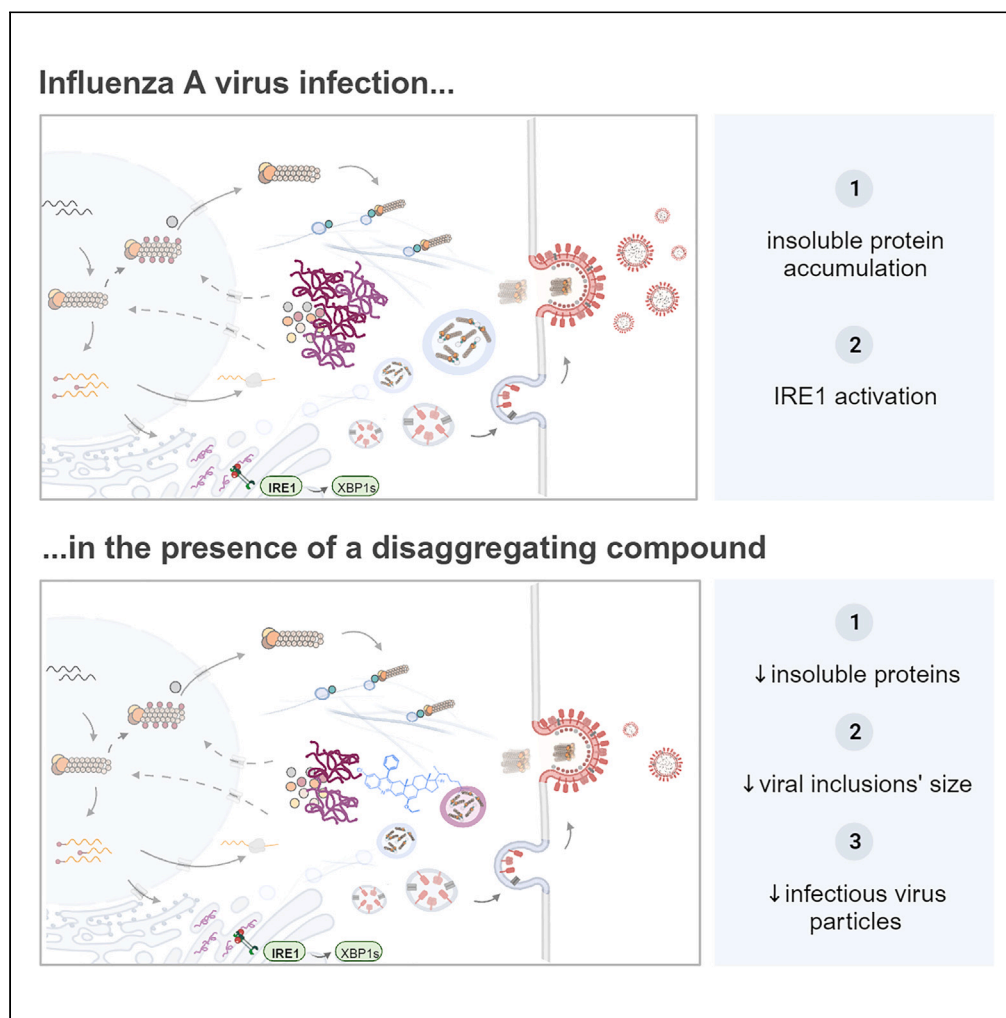**Article**

Influenza A virus propagation requires the activation of the unfolded protein response and the accumulation of insoluble protein aggregates

Influenza A virus infection...

1. insoluble protein accumulation
2. IRE1 activation

...in the presence of a disaggregating compound

1. ↓ insoluble proteins
2. ↓ viral inclusions' size
3. ↓ infectious virus particles

Mariana Marques, Bruno Ramos, Hélio Albuquerque, ..., Artur M.S. Silva, Ana Raquel Soares, Daniela Ribeiro

daniela.ribeiro@ua.pt

Highlights

IAV requires the specific activation of the UPR IRE1 branch to effectively replicate

IAV induces the accumulation of insoluble protein aggregates

Virus-induced insoluble aggregates contain host and viral proteins

Chemical targeting of the virus-induced aggregates prevents viral assembly

Article

Influenza A virus propagation requires the activation of the unfolded protein response and the accumulation of insoluble protein aggregates

Mariana Marques,[1] Bruno Ramos,[1] Hélio Albuquerque,[2] Marisa Pereira,[1] Diana Roberta Ribeiro,[1] Alexandre Nunes,[1] Jéssica Sarabando,[1] Daniela Brás,[3] Ana Rita Ferreira,[1] Rui Vitorino,[1] Maria João Amorim,[3,4] Artur M.S. Silva,[2] Ana Raquel Soares,[1,5] and Daniela Ribeiro[1,5,6,*]

SUMMARY

Influenza A virus (IAV) employs multiple strategies to manipulate cellular mechanisms and support proper virion formation and propagation. In this study, we performed a detailed analysis of the interplay between IAV and the host cells' proteostasis throughout the entire infectious cycle. We reveal that IAV infection activates the inositol requiring enzyme 1 (IRE1) branch of the unfolded protein response, and that this activation is important for an efficient infection. We further observed the accumulation of virus-induced insoluble protein aggregates, containing both viral and host proteins, associated with a dysregulation of the host cell RNA metabolism. Our data indicate that this accumulation is important for IAV propagation and favors the final steps of the infection cycle, more specifically the virion assembly. These findings reveal additional mechanisms by which IAV disrupts host proteostasis and uncovers new cellular targets that can be explored for the development of host-directed antiviral strategies.

INTRODUCTION

Viruses have developed multiple strategies to hijack and control host cellular activities to evade the immune response and support efficient virus particle production. Some of these strategies include the manipulation of cytoplasmic and endoplasmic reticulum (ER)-related mechanisms involved in protein metabolism.[1–3] To counteract disturbances in the proteome and re-establish basal homeostasis, cells have evolved distinct surveillance mechanisms concerning protein biogenesis, folding, degradation, and sequestration of abnormal and potentially pathogenic conformers.[4] One of the most important mechanisms for protein stress detection is the ER unfolded protein response (UPR).[5] Upon activation of one or more of the key UPR signal activator proteins (inositol requiring enzyme (IRE1), protein kinase R (PKR)-like ER kinase (PERK) and activating transcription factor 6 (ATF6)), downstream signaling leads to the attenuation of general protein synthesis with selective protein translation (via PERK), preferential degradation of mRNA encoding for ER-localized proteins (via IRE1), and the controlled synthesis of stress-attenuating proteins, such as chaperones and folding catalysts (via PERK, IRE1 and ATF6).[6] The ER-associated protein degradation (ERAD) pathway may also be activated, allowing the clearance of misfolded and accumulated proteins in the ER.[7] Various cytoplasmic chaperones, such as heat shock proteins (HSPs), also assist the folding and assembly of newly synthesized and stress-damaged proteins, to prevent potentially pathogenic protein aggregation.[8] Misfolded or aggregated proteins may also be sequestered and compartmentalized into stress foci to hinder their toxic effects and minimize interference.[9]

Several viruses lead to the accumulation of protein aggregates in specialized compartments, generally termed virus factories, in order to recruit and concentrate viral and host components and facilitate the molecular interactions required for essential steps of genome replication or virus particle assembly, while escaping immune recognition.[10] As part of the host antiviral response to infection, cytoplasmic aggregates, comprising both host and viral components, can also be formed and eventually become targeted for degradation to facilitate viral clearance and cellular recovery.[11]

The importance of protein homeostasis in the context of viral infections is well recognized, supporting that further efforts to understand the underpinning molecular mechanisms may lead to antiviral control. With that in mind, in this work, we performed a detailed analysis of different proteostasis-related mechanisms in the course of influenza A virus (IAV) infection. IAV is the causative agent of most of the annual respiratory epidemics in humans,[12] with a high level of morbidity and mortality in the elderly and individuals with chronical disease conditions.[13] IAV

[1]Institute of Biomedicine – iBiMED, Department of Medical Sciences University of Aveiro, Aveiro, Portugal
[2]LAQV-REQUIMTE, Department of Chemistry, University of Aveiro, Campus de Santiago, 3810-193 Aveiro, Portugal
[3]Instituto Gulbenkian de Ciência, 2780-156 Oeiras, Portugal
[4]Católica Biomedical Research Centre, Católica Medical School, Universidade Católica Portuguesa, 1649-023 Lisboa, Portugal
[5]These authors contributed equally
[6]Lead contact
*Correspondence: daniela.ribeiro@ua.pt
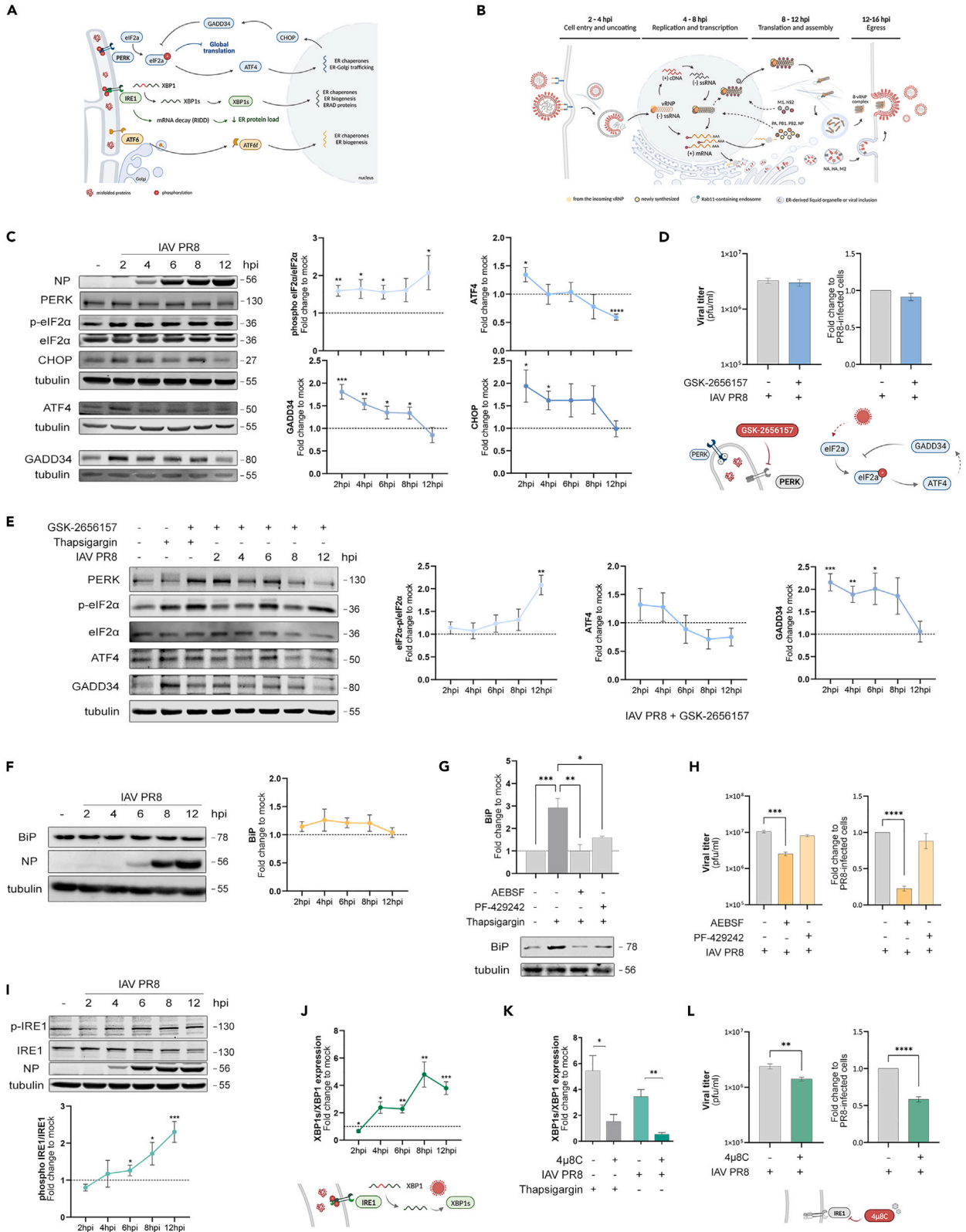https://doi.org/10.1016/j.isci.2024.109100

Figure 1. Analysis of the host cell UPR during IAV infection

(A) Schematic representation of the three main branches of UPR in the ER.

(B) Schematic representation of the influenza A virus life cycle. Important steps in infection are indicated with the usual time frames post infection in A549 cells.

(C–E) Analysis of the relevance of the UPR PERK branch during infection with IAV in A549 cells.

(C) Western blot analysis of the expression levels of PERK, p-eIF2α/eIF2α, CHOP, ATF4 and GADD34 proteins in A549 cells, following IAV PR8 infection at different times post infection. Tubulin was used as internal control. Data represents the means ± SEM of three independent experiments.

(D) Similar analyses as in C, but in the presence of 0.33 µM of the PERK inhibitor GSK-2656157. 500 nM thapsigargin treatment for 8 h served as positive control for PERK activation. Quantification values were normalized to mock and represent average ± SEM of at least three independent experiments. Tubulin was used as internal control.

(E) Plaque assay analysis of the viral titer obtained upon IAV PR8 infection of A549, in the presence or absence of 0.33 µM GSK-2656157. Data represents the means ± SEM of three independent experiments.

(F–H) Analysis of the relevance of the UPR ATF6 branch during infection with IAV in A549 cells.

(F) Western blot analysis of the expression of BiP protein in A549 infected with IAV PR8 at various times post-infection and (G) upon stimulation with 500 nM thapsigargin for 8 h, in the presence of 0.1 mM AEBSF or 30 µM PF-429242 (ATF6 inhibitors). Data represents the means ± SEM of three independent experiments.

(H) Plaque assay analysis of the viral titer of A549 cells infected with IAV PR8 in the presence or absence of 0.1 mM AEBSF or 30 µM PF-429242. Data represents the means ± SEM of three independent experiments.

(I–L) Analysis of the relevance of the UPR IRE1 branch during infection with IAV in A549 cells.

(I) Western blot analysis of the expression levels of the phosphorylated and total forms of the IRE1 protein at different times post infection. Quantification values were normalized to mock-infected cells and tubulin was used as internal control. Data represents the means ± SEM of three independent experiments.

(J) RT-qPCR analysis of the splicing of XBP1 at different times post infection in relation to mock-infected cells and (K) upon stimulation with thapsigargin or infected with IAV PR8, in the presence or absence of 20 µM 4µ8C (IRE1 inhibitor), in relation to untreated cells. Data represents the means ± SEM of three independent experiments.

(L) Plaque assay analysis of the viral titer obtained upon IAV PR8 in the presence or absence of 4µ8C. Data represents the means ± SEM of at least three independent experiments. *p < 0.005, **p < 0.001, ***p < 0.0001, ****p < 0.00001 using Student's t test. See also Figure S1.

belongs to the *Orthomyxoviridae* family, featuring a segmented genome composed by eight single-stranded negative-sense linear RNA segments, separately enclosed and wrapped by the viral nucleoprotein (NP) in the form of viral ribonucleoprotein complexes (vRNPs).[14] Upon successful binding to the host cell membrane, IAV virions are internalized, and its genome is released into the cytoplasm, being further imported to the nucleus where it undergoes transcription and replication.[15] The translation of viral proteins at the cytoplasmic and ER-associated ribosomes, together with the formation of vRNPs in the nucleus, culminate in the assembly of progeny virions that bud at the plasma membrane before being released from the cell.[15]

Not much is known concerning the interplay between IAV and the host cell proteostasis, and the available information is somewhat contradictory. Regarding the UPR, while some authors reported the activation of the ATF6 pathway upon IAV infection[16] and others suggested the inhibition of PERK as a possible IAV antiviral strategy,[17] additional studies have described the stimulation of the IRE1 branch upon infection[18–21] with little or no concomitant activation of the ATF6 and PERK branches.[20,21]

These variances may, however, be related to the use of different cell models and/or viral strains. Nevertheless, the UPR has been suggested as a putative target for host-directed antivirals against IAV infection, as its activation by thapsigargin has been shown to block viral replication.[22] More recently, UPR activation mediated by thiopurines led to the selective disruption of the synthesis and maturation of IAV glycoproteins HA and NA, eventually blocking viral replication.[23] Some studies have described the accumulation of IAV-derived amyloid-like fibers to induce cytotoxicity,[24] as well as the formation of aggresome-like structures in IAV-infected dendritic cells to evade the immune response.[25] It has also been shown that the accumulation of cytosolic stress granules, usually formed upon different kinds of cellular stress, is prevented upon IAV infection.[26]

To clarify how the host cell proteostasis impacts IAV infection, we evaluated how specific proteostasis-related mechanisms are affected throughout the main phases of a single IAV infectious cycle. Our results not only demonstrate that IAV interferes with the UPR at different stages of infection, mainly through its IRE1 branch, but also that this interplay is required for proper virus particle formation and propagation. Importantly, we demonstrate that, upon high rates of viral protein translation, IAV induces the accumulation of insoluble protein aggregates at the cytosol composed of both host and viral proteins. By chemically disrupting the assembly of these protein aggregates, we demonstrate that this process is essential for efficient viral protein production and proper formation of infectious virus particles, supporting the idea that targeting proteostasis-related mechanisms may constitute a valid therapeutic approach to tackle and decrease viral propagation.

RESULTS

Influenza A virus triggers the IRE1 branch of the unfolded protein response to ensure efficient viral propagation

To elucidate which UPR pathways are specifically activated or remodeled throughout the different steps of the virus infectious cycle, we performed a detailed analysis of the distinct UPR signaling pathways (depicted in Figure 1A) at different time points during a single cycle of infection. This comparative approach allowed assessing the interplay between infection and host proteostasis mechanisms and its potential to be used as a therapeutic target.

Adenocarcinomic human alveolar basal epithelial (A549) cells were infected with influenza A/Puerto Rico/34/8 (IAV PR8)[27,28] and UPR-related genes or proteins were assessed at different time-points post infection, reflecting the most relevant steps of the virus life cycle (depicted

in Figure 1B), namely 2, 4 6, 8 and 12 hpi. To investigate the PERK UPR branch, we evaluated the expression/activation of several proteins belonging to this pathway, namely eIF2α, ATF4, CHOP and GADD34. eIF2α, which catalyzes an early step of protein synthesis initiation, becomes phosphorylated upon PERK activation to induce global translation arrest, while allowing the selective translation of different proteins such as ATF4.[5] ATF4 further induces both CHOP and GADD34 expression to ultimately counteract eIF2α phosphorylation in a negative loop to restore translation levels (Figure 1A). Quantification of the expression ratio between the phosphorylated and unphosphorylated eIF2α (Figure 1C) showed an increase in eIF2α phosphorylation already at 2 hpi, being this activation maintained throughout the remaining infection cycle, as reported by others.[29] ATF4 expression increases at the initial steps of infection and decreases thereafter (Figures 1C and S1A). Similarly, the expression of both CHOP and GADD34 increases at early time points and subsequently decreases progressively until the end of infection (Figure 1C), although maintaining a higher level than in uninfected (mock) cells. However, the characteristic band smear that indicates PERK activation is not detected by Western blotting upon infection (Figure 1C). To further elucidate the importance of the PERK pathway for IAV infection, cells were infected with IAV PR8 in the presence of a specific inhibitor of PERK, GSK-2656157 (as in[30]). Upon assessment of the amount of infectious virus particles produced in the presence and absence of this inhibitor, our results clearly indicate that PERK inhibition does not affect virus production (Figure 1D). In addition, upon infection, eIF2α phosphorylation is still observed upon incubation with the PERK inhibitor, and the expression levels of ATF4 and GADD34 are also maintained (Figures 1C and 1E). Overall, this indicates that the observed eIF2α phosphorylation upon IAV infection is unlikely to result from PERK activation, but rather from the activation of another kinase.

To analyze the relevance of the UPR ATF6 pathway for IAV infection, we measured the BiP/grp78 protein and mRNA levels, previously suggested to serve as an indirect measure of ATF6 activation.[31,32] Our results demonstrate no alteration of BiP/grp78 levels (Figures 1F, S1A, and S1B), suggesting that the ATF6 branch is not required during infection with IAV. To validate this observation, we infected the cells upon incubation either with a broad-spectrum serine protease inhibitor commonly used to inhibit ATF6, 4-(2-aminoethyl) benzenesulfonyl fluoride (AEBSF) (as in[20,33]), or PF-429242,[32] which targets the SP1 enzyme that cleaves ATF6 in the Golgi (Figure 1G). Quantification of the formation of infectious virus particles by plaque assay demonstrated a significant decrease in the number of new virus particles upon inhibition of the ATF6 pathway with AESBF, but not with PF-429242 (Figure 1H). Altogether, and considering that AESBF has a less specific and wider activity, these data suggest that ATF6 is not relevant for the efficient replication and propagation of IAV. Lastly, the activation of the IRE1 pathway was assessed via the phosphorylation of IRE1 and the splicing of XBP1. We observed an increase in the phosphorylation of IRE1 starting at 6 hpi up to 12 hpi with IAV PR8 (Figures 1I and S1B), reflecting a stage of the life cycle where viral proteins are actively being translated. Coherently, the levels of spliced XBP1 were significantly increased, (Figure 1J), particularly at 8 hpi. In this case, cells treated with thapsigargin were used as a positive control, with a value of XBP1 splicing of 7.51 ± 1,35 (mean ± SEM). To further infer the importance of this activation for viral propagation, we have quantified infectious virus particle formation in the presence of a specific inhibitor of this pathway, 4μ8C (as in[20,34]) (Figures 1K and 1L). In the presence of this inhibitor, virus production was attenuated by approximately 40% (Figure 1L), indicating that the activation of the UPR IRE1 branch by IAV is important for IAV particle formation and propagation.

Collectively, our data indicate that UPR activation occurs at different stages of infection, and that an efficient IRE1 pathway activation is required for the proper disenrollment of the IAV PR8 infection cycle.

Influenza A virus induces the accumulation of cytosolic protein aggregates

We proceeded our study by analyzing whether IAV infection leads to proteostasis imbalances through the accumulation of insoluble proteins. A549 cells were infected with IAV PR8 and samples were harvested to further analyze the detergent-insoluble protein fractions by SDS-PAGE, as previously reported.[35] Insoluble proteins accumulate in cells infected with IAV (Figure 2A), particularly at 8 hpi when a considerable amount of the viral RNA has been transcribed and replicated, viral transcripts and viral progeny RNA (in the form of vRNPs) have exited the nucleus, and a substantial amount of viral proteins is being synthesized. Our results indicate proteostasis impairment and overlap with the activation of the IRE1 pathway. This effect appears to be reversible at later times post-infection (Figure 2A).

Aiming at visualizing and intracellularly localizing these protein aggregates, we stained A549 infected cells with Proteostat, a dye that specifically marks for misfolded and aggregated proteins (Figure 2B). At 8 hpi, Proteostat stains several cytoplasmic protein aggregates (Figure 2B), in approximately 53% ± 5.7% of the infected cells, mainly localized at the perinuclear area. To solidify these results, we have performed the same experiment in another cell type, a previously established HeLa cell line that stably expresses a GFP-tagged protein misfolding sensor HSPB1:GFP (HeLa HSPB1:GFP cells).[36] Similarly to A549 cells, the formation of several cytoplasmic protein aggregates stained by both Proteostat and HSPB1:GFP was observed (Figure 2C), in approximately 38% ± 0.6% of the infected cells. Cellular proteins that are prone to aggregate are usually aberrant and targeted for degradation or tend to accumulate in cytosolic stress granules and promote the conversion into aberrant aggresome-like structures. With this in mind, and aiming to further characterize the virus-induced protein aggregates detected by the Proteostat dye, we have analyzed for the amount of mono- and polyubiquitinated proteins (stained with FK2 antibody), stress granules formation (with TIA-R), using specific stressors as positive controls, as well as autophagic activity (with p62) at a time of the infection when we observed the formation of Proteostat-stained aggresomes. We found that the mono and polyubiquitination of cytoplasmatic proteins (Figure S2A) increases during infection, but it does not colocalize with Proteostat staining. Lastly, we also demonstrated that the observed aggregates do not correspond to stress granules (Figure S2B). Lastly, p62 foci seem to be inhibited during infection (Figure S2C) and it does not resemble the formation of IAV-induced aggresomes. Altogether, these results reveal that IAV induces the formation of cytoplasmic protein aggregates, at a time point of the infection cycle where an intense production of viral proteins is occurring,[37] as well as the activation of the UPR IRE1 pathway.
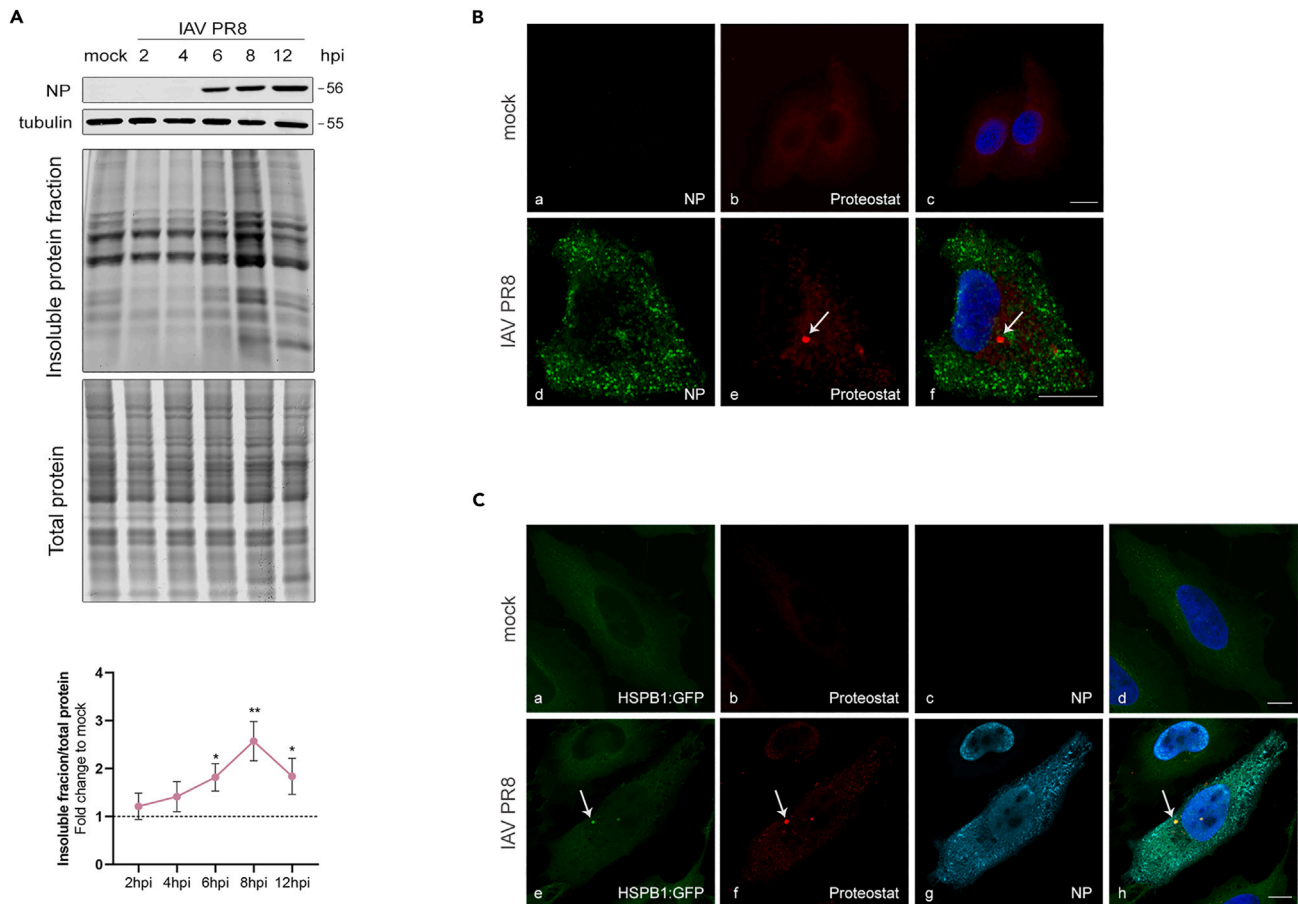
Figure 2. Analysis of the accumulation of misfolded proteins in IAV-infected cells

(A) Characterization of the insoluble protein fraction of A549 cells infected with IAV PR8 at different times post infection. Data represents means ± SEM of at least independent experiments, *p < 0.05, ****p < 0.0001 using Student's *t* test.

(B) Aggresomes formation in mock- or IAV PR8-infected A549 cells at 8 hpi. Confocal images of (a, d) viral NP, (b, e) Proteostat dye and (c, f) merge image.

(C) Aggresomes formation in mock- or IAV PR8-infected in HeLa HSPB1:GFP cells at 8 hpi. Confocal images of (a, e) endogenous HSPB1:GFP, (b, f) Proteostat dye, (c, g) anti-NP and (d, h) merge images. Arrows indicate the presence of aggresome-like structures. Bars represent 10 μm. See also Figure S2.

The insoluble protein fraction of infected cells contains viral proteins and is enriched in host translation-related proteins

To obtain further insights on the composition of these protein aggregates, we performed liquid chromatography-tandem mass spectrometry analysis (LC-MS/MS) of the detergent-insoluble protein fraction of mock and IAV PR8-infected cells at 8 hpi (Figure 3A).

Five viral proteins were found in the insoluble protein fraction of infected cells, namely the RNA-directed RNA polymerase catalytic subunit (PB1), matrix protein 1 (M1), nucleoprotein (NP), non-structural protein 1 (NS1) and polymerase basic protein 2 (PB2) (Table S1). A total of 156 and 263 human proteins were identified with at least two unique peptides in mock and IAV PR8-infected cells, respectively (Table S2), corroborating our previous results that show an increase in the level of insoluble proteins at this stage of infection. Of the identified proteins, 123 were solely found in the insoluble fraction of cells infected with IAV PR8 (Figure 3B). A gene ontology analysis using the Cytoscape plug-in ClueGo revealed that these proteins belong to a specific set of biological processes related to translation, mRNA splicing and the ribonucleoprotein complex biogenesis (Figure 3B).

Through a complementary analysis, we determined which host insoluble proteins were enriched in IAV PR8-infected cells in comparison to non-infected cells. Proteins with an abundance ratio (IAV PR8 to mock) greater than 1.5 with an adjusted p value smaller than 0.05 were considered enriched. This analysis allowed the identification of 78 host proteins whose abundance is increased in the insoluble protein fraction upon infection (Table S3). Gene ontology analysis using Cytoscape showed that these proteins are involved essentially in processes related to ribonucleoprotein complex export from the nucleus, mRNA stabilization, but also in processes such as the regulation of mitophagy, or the tricarboxylic acid metabolism (Figure 3C; Table S4A). An extra analysis using STRING database showed that our network of proteins enriched in the insoluble fraction of IAV PR8-infected cells are related to nuclear DNA replication, ribonucleoprotein export from the nucleus and several processes related to RNA metabolism (Table S4B).
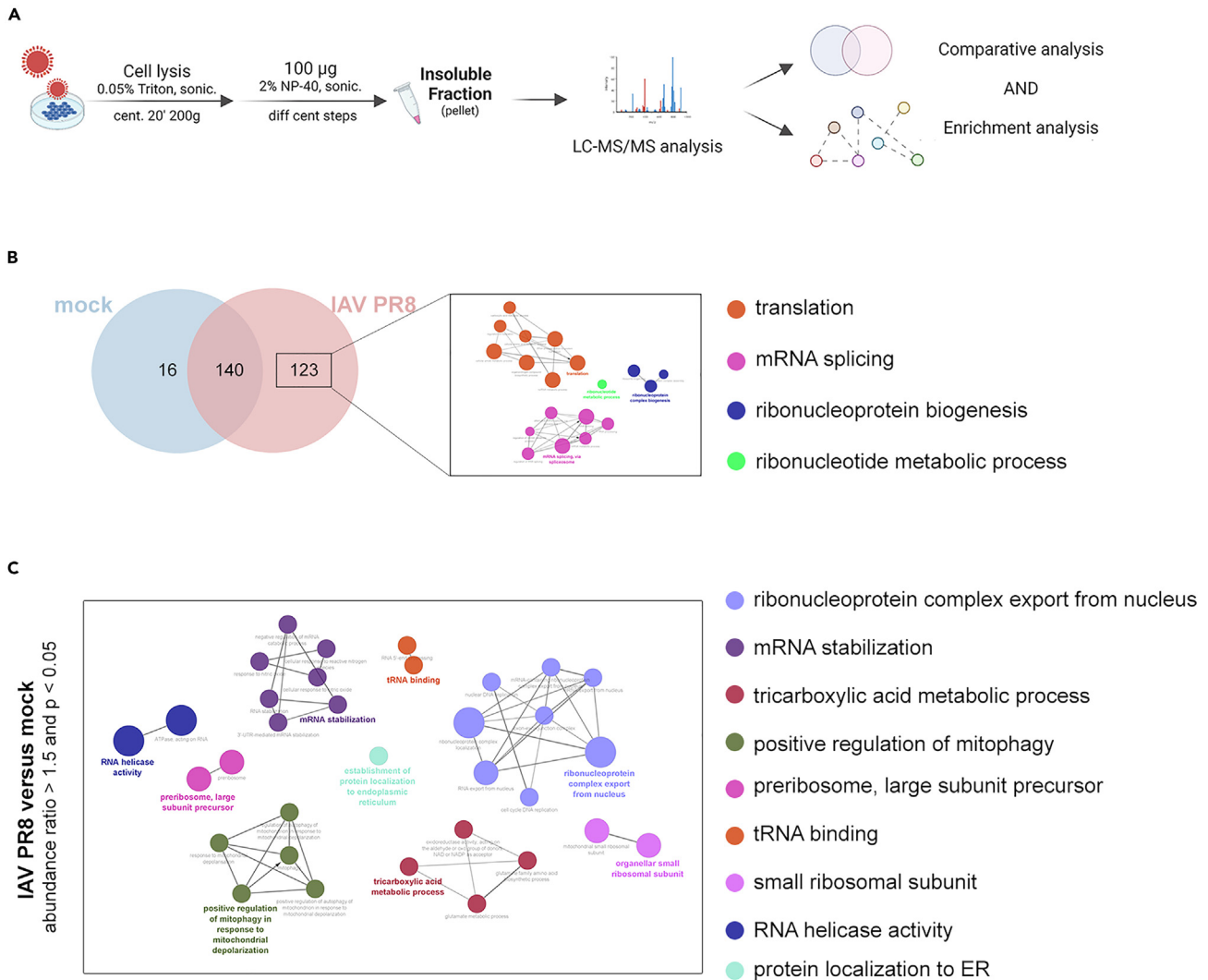
Figure 3. Analysis of the host proteins present in the insoluble fraction of infected cells by LC-MS/MS

(A) Experimental approach used to isolate and characterize the insoluble protein fraction. (B-C) Comparison between the insoluble protein fractions in IAV PR8-and mock-infected cells.

(B) Venn diagram representing the number of host's proteins identified in the insoluble fractions from IAV PR8-infected and non-infected cells. Characterization of insoluble proteins found solely in the insoluble fraction of IAV PR8-infected cells using the ClueGo plugin in Cytoscape, based on the results from the LC-MS/MS analysis of three independent experiments. For this analysis, proteins identified by peptides and unique peptides >2 in at least 2 experiments were considered.

(C) Gene ontology analysis (using ClueGO) of the enriched insoluble proteins in IAV PR8-infected cells. See also Tables S1–S4.

These results indicate that the solubility of several host proteins related to protein translation and RNA processing is altered at this time point of infection. Whether this occurs to benefit viral infection or as a host strategy to counteract infection is still unclear.

Viral and host proteins found to be enriched in the insoluble fraction of IAV PR8-infected samples in comparison to mock (Tables S1 and S3) were then accessed for their natural propensity to aggregate, using PASTA 2.0,[38] a web server for the prediction of protein aggregation propensity by determining fibril formation. Beta-amyloid and bovine serum albumin (BSA) were used respectively as positive and negative controls of aggregation propensity and to define the threshold of best energy values for further comparison analyses. As depicted in Table 1, all IAV proteins identified in the insoluble fractions of infected cells have no propensity to aggregate, namely PB1, M1, NP, NS1 and PB2. On the other hand, only 10 of the 78 proteins from the host have shown to have propensity to aggregate (defined as having best energy < −11), which corresponds to 12.8% of the detected host proteins in this fraction. Although there is no functional enrichment identified among these 10 proteins, meaning they are not commonly related to any specific cellular mechanism, our results indicate that most of the detected proteins in the insoluble fractions of infected cells are indeed accumulating as a result of the viral infection.

Table 1. Aggregation prediction of host's and influenza A virus' (in bold) proteins identified in the insoluble fractions of infected cells using PASTA 2.0

Identifier	Gene Symbol	Protein name	Best energy
O96005	CLPTM1	Cleft lip and palate transmembrane protein 1	−29.58
P03468	**NA**	**Neuraminidase**	**−24.21**
P05067	Beta-amyloid (positive control)		−20.17
Q8WVX9	FAR1	Fatty acyl-CoA reductase 1	−19,19
P27105	STOM	Stomatin	−17,66
P29317	EPHA2	Ephrin type-A receptor 2	−15,36
O95831	AIFM1	Apoptosis-inducing factor 1, mitochondrial	−15,13
M0QXM4	SLC1A5	Amino acid transporter	−14,60
P06821	**M2**	**Matrix protein 2**	**−14.52**
O95140	MFN2	Mitofusin-2	−13,67
H0Y714	IMP4	U3 small nucleolar ribonucleoprotein protein IMP4	−13,40
P03452	**HA**	**Hemagglutinin**	**−13.07**
Q8TEM1	NUP210	Nuclear pore membrane glycoprotein 210	−12,66
Q02880	TOP2B	DNA topoisomerase 2-beta	−11,07
Defined cut-off for protein propensity to aggregate			
A0A494C0A8	*TBK1*	*Serine/threonine-protein kinase 1*	*−10,97*
B9ZVN9	*POLR1A*	*DNA-directed RNA polymerase subunit*	*−10,83*
H0Y368	*DPM1*	*Dolichol-phosphate mannosyltransferase subunit 1*	*−10,40*
H0Y3P2	*EIF4G2*	*Eukaryotic translation initiation factor 4 gamma 2*	*−10,27*
O00203	*AP3B1*	*AP-3 complex subunit beta-1*	*−10,17*
P13667	*PDIA4*	*Protein disulfide-isomerase A4*	*−9,48*
P83111	*LACTB*	*Serine beta-lactamase-like protein LACTB*	*−9,45*
C9J2Y9	*POLR2B*	*DNA-directed RNA polymerase subunit beta*	*−9,37*
Q12769	*NUP160*	*Nuclear pore complex protein Nup160*	*−9,28*
Q8NBQ5	*HSD17B11*	*Estradiol 17-beta-dehydrogenase 11*	*−9,18*
P02769	BSA (negative control)		−9.09
P03428	**PB2[#]**	**Polymerase basic protein 2**	**−8.67**
P03485	**M1[#]**	**Matrix protein 1**	**−8.09**
P03496	**NS1[#]**	**Non-structural protein 1**	**−7.92**
P03431	**PB1[#]**	**RNA-directed RNA polymerase catalytic subunit**	**−7.62**
P03466	**NP[#]**	**Nucleoprotein**	**−4.95**

Beta-amyloid and BSA were used as a positive of negative control, respectively. Host proteins with best energy values higher than BSA but below cut-off are italic; host proteins with best energy values below BSA are not represented. # refers to viral proteins found in the insoluble protein fraction of infected cells.

The formation of IAV-induced protein aggregates favors infection

To understand if the observed virus-induced accumulation of insoluble protein aggregates is relevant for the process of virus particle formation, we disturbed the assembly of these aggregates and analyzed its consequence for viral propagation. For that, we used HASQ-6Cl ($C_{42}H_{52}ClNO$, ^1H and ^{13}C-NMR spectra (Figure S3), a steroid-quinoline hybrid that has been shown to disrupt and revert protein aggregation processes (named 6c in[39]) (Figure 4A). This compound was tested for cell viability and toxicity and the ideal experimental concentration was determined (Figure S3).

A549 cells were treated with 50 μM of HASQ-6Cl 12 h prior to infection with IAV PR8 and harvested at 8 hpi (the time point after infection where we observed a higher accumulation of insoluble proteins) to analyze the insoluble protein fraction. The virus-induced levels of insoluble proteins decreased around 50% in the presence of HASQ-6Cl (Figure 4B), demonstrating that this compound is also able to inhibit the formation of IAV-induced protein aggregates. The effect of this protein aggregation-inhibition on IAV infectious particle formation was analyzed by plaque assay at 16 hpi. A decrease of around 50% in the number of infectious viral particles in the presence of HASQ-6Cl was observed (Figure 4C), indicating that the virus infection cycle is disturbed by the disaggregating compound.
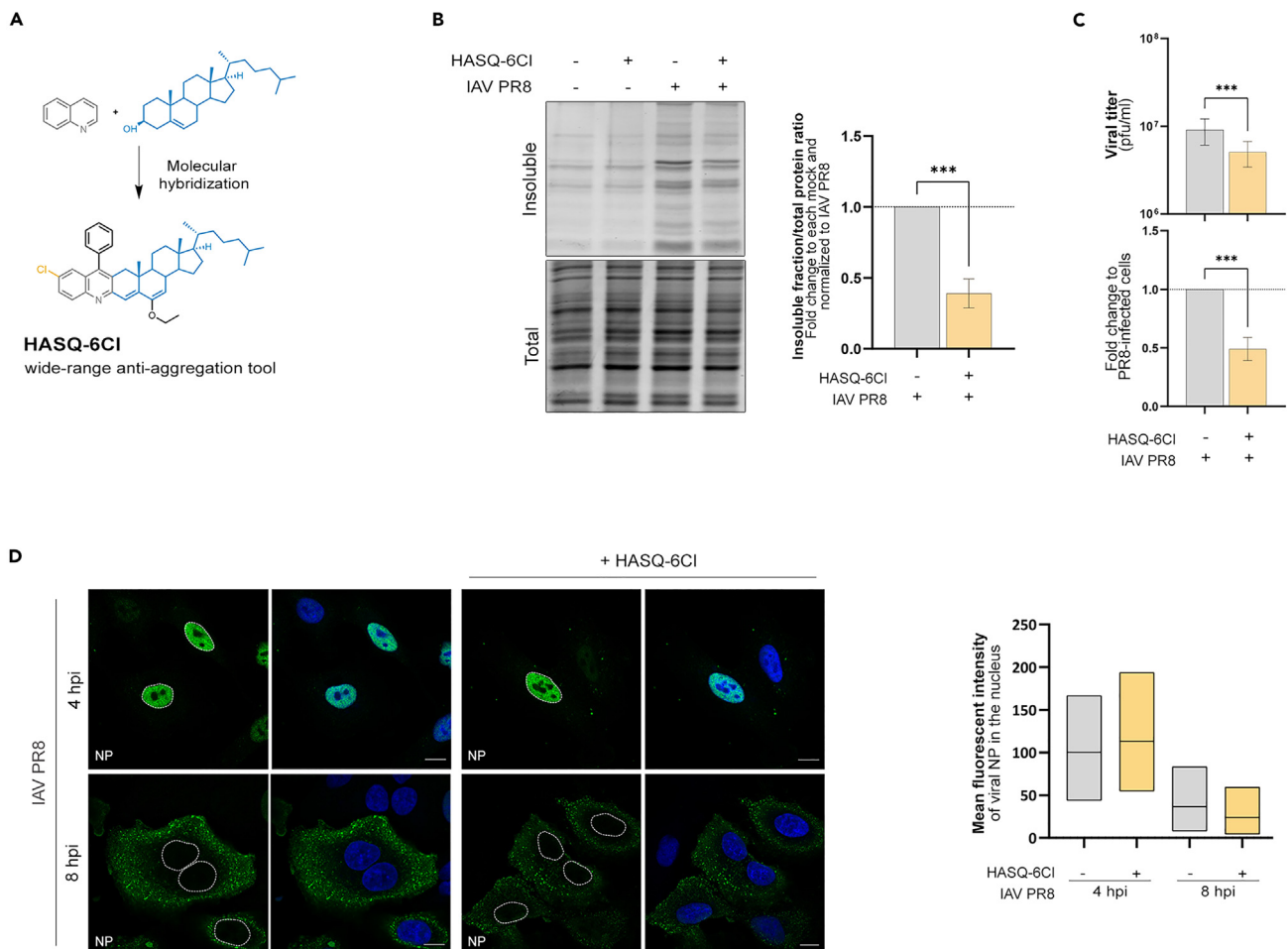
Figure 4. Importance of protein aggregation for IAV propagation

(A) Simplified representation of the molecular hybridization reaction used to synthesize HASQ-6Cl. The combination of quinolines (in gray) and steroids (in blue) in one new chemical entity, generates a hybrid molecule with wide-range of anti-aggregation functions.

(B) Analysis of the insoluble fraction of A549 cells infected for 8 h with IAV PR8 in the absence or presence of HASQ-6Cl. The final ratios were obtained by first normalizing the intensity of insoluble proteins fractions to the intensity of total fraction, followed by its normalization to the correspondent mock, and finally its normalization to IAV PR8. Data represents the means $\pm$ SEM of three independent experiments.

(C) Viral titers of IAV PR8 after treatment of A549 cells with HASQ-6Cl. Values were normalized to IAV PR8 and represent average $\pm$SEM of at least three independent experiments, ***p < 0.001, in Student's *t* test.

(D) Confocal images of A549 cells infected with IAV PR8 for 4 h and 8 h in the absence or in the presence of HASQ-6Cl. Viral NP is stained in green and nuclei are in blue (DAPI). Bars represent 10 μm. Data represents the mean fluorescence intensity of viral NP in the nucleus as box and whiskers min to max of three independent experiments, ****p < 0.0001 using ordinary one-way ANOVA followed by Bonferroni's multiple comparisons test. See also Figure S3.

To infer the specific infection step that was affected by the compound, we analyzed the viral NP mean fluorescence intensity (MFI) in the nucleus of IAV PR8-infected A549 cells, in the presence and absence of HASQ-6Cl. Our results indicate that the amount of nuclear NP is not affected by HASQ-6Cl at 4 or 8 hpi (Figure 4D) and further show that HASQ-6Cl does not interfere either with the IAV entry into the cell or with the export of vRNPs from the nucleus at later times post-infection, suggesting a downstream effect on the viral life cycle.

Although these results cumulatively suggest that the formation of these protein aggregates may be a virus-induced mechanism to favor viral protein production, one should also hypothesize whether the decrease in virus titer in the presence of HASQ-6Cl could also result from its effect on a host mechanism that further impairs viral infection. As we had previously demonstrated that the activation of the UPR IRE1 branch is relevant for proper IAV particle formation, we questioned whether HASQ-6Cl would exert some effect over this pathway and consequently cause the observed decrease in virus titers. To investigate this hypothesis, we measured the splicing of XBP1 mRNA upon 8 h of infection with IAV PR8 in the presence or absence of HASQ-6Cl. Figure 5A shows that there were no observed differences in XBP1 splicing in the presence of HASQ-6Cl, demonstrating that the compound has no effect on the level of IRE1 pathway induction by the virus. Our results also show no significant changes in the level of eIF2α phosphorylation or BiP expression throughout infection in the presence of HASQ-6Cl (Figure 5B).
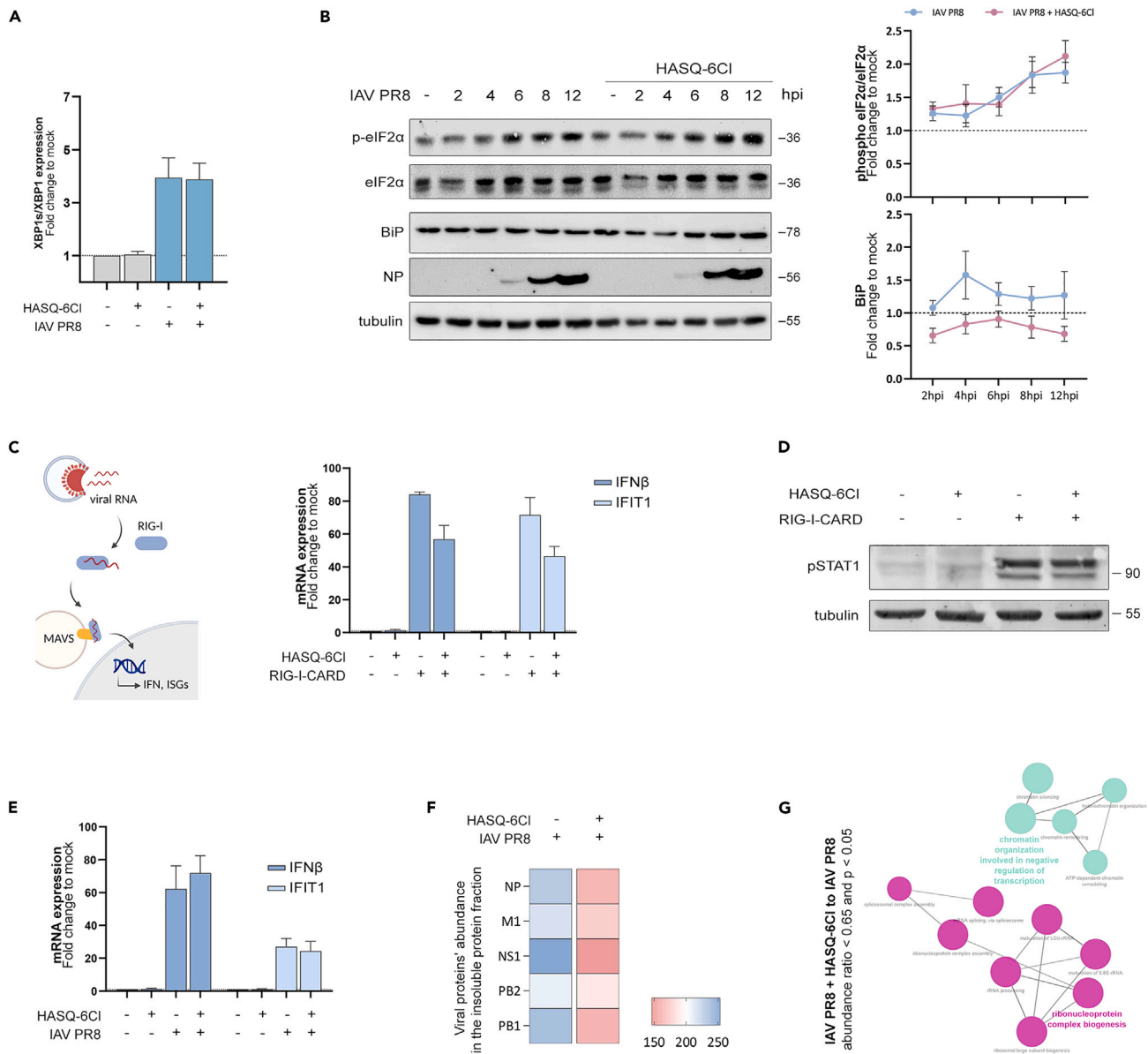
Figure 5. Analysis of effect of HASQ-6Cl on the host cell's immune response and UPR signaling

(A) RT-qPCR analysis of the splicing of *XBP1* mRNA in A549 cells infected with IAV PR8 for 8 h in the absence or in the presence of HASQ-6Cl, in relation to mock-infected cells. Data represents the means ± SEM of three independent experiments. *p < 0.05 in two-way ANOVA, with Bonferroni's comparison test.

(B) Western blot analysis of eIF2α phosphorylation and BiP expression in A549 cells infected with IAV PR8 at different times post infection in the absence or in the presence of HASQ-6Cl. Tubulin was used as internal control. Data represents the means ± SEM of three independent experiments.

(C–E) Analysis of the effect of HASQ-6Cl on the innate immune response.

(C) RT-qPCR analysis of the IFNβ mRNA expression in A549 cells after stimulation with RIG-I-CARD for 10 h in the absence or in the presence of HASQ-6Cl, normalized to control. Data represents the means ± SEM of three independent experiments.

(D) Western blot analysis of pSTAT1 activation following A549 cells stimulation with RIG-I-CARD for 10 h in the absence or in the presence of HASQ-6Cl. I RT-qPCR analysis of the IFNβ mRNA expression in A549 cells after infection with IAV PR8 for 8 h in the absence or in the presence of HASQ-6Cl. Data represents the means ± SEM of three independent experiments.

(F) Viral proteins' abundance in the insoluble fraction of A549 cells infected with IAV PR8 in the presence or absence of HASQ-6Cl. Color gradient represents the relative abundance of each viral protein in comparison to other viral proteins' abundances, considering both samples, from the lowest (red) to the highest (blue) value.

(G) Characterization of the insoluble protein fraction of IAV PR8-infected cells in the presence of HASQ-6Cl. GO term analysis (using ClueGO) of the diminished insoluble proteins in cells infected with IAV PR8 after HASQ-6Cl treatment versus IAV PR8-infected cells (abundance ratio <0.65 and p value <0.05 considering three biological replicates).
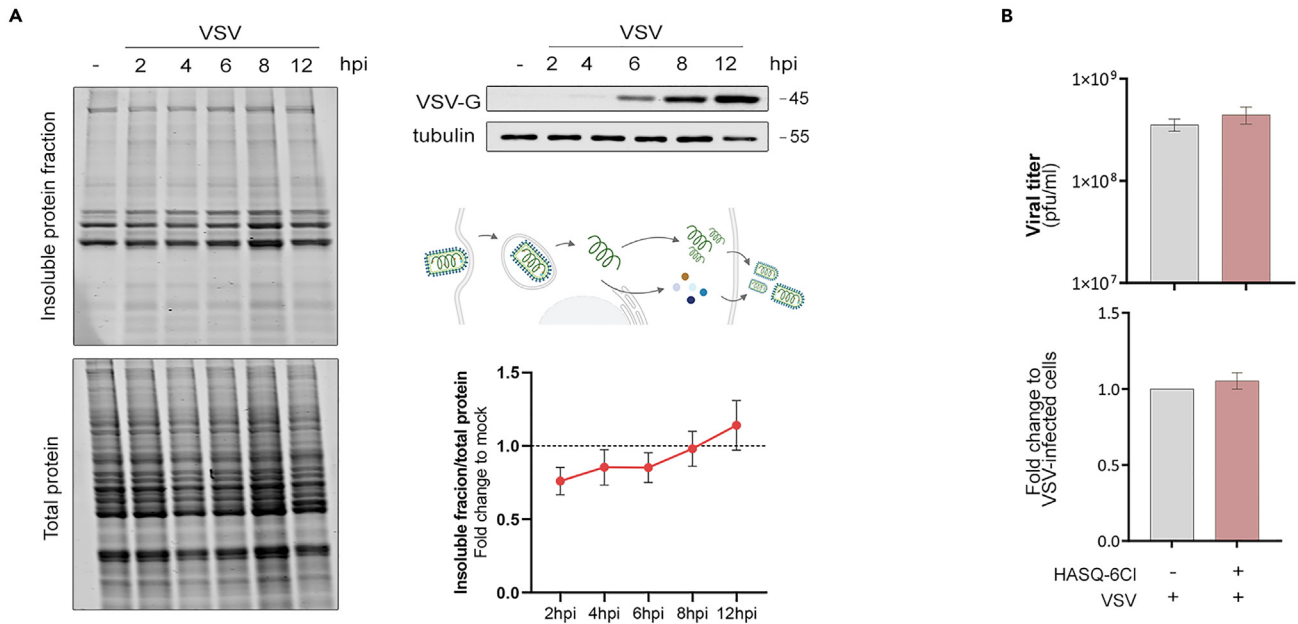
Figure 6. Analysis of the accumulation of misfolded proteins in VSV-infected cells

(A) Characterization of the insoluble protein fraction of A549 cells infected with VSV at different times post infection.

(B) VSV titers after treatment of A549 cells with HASQ-6Cl. Values were normalized to IAV PR8. Data represents means ± SEM of at least independent experiments, *p < 0.05, ****p < 0.0001 using Student's t test.

Another possibility might be that this compound could, by itself, induce the improvement of the cellular antiviral response against IAV. As most RNA viruses, IAV is mainly sensed by the RIG-I/MAVS antiviral signaling pathway,[40] which culminates in the production of interferons (IFNs) or IFN-stimulated genes (ISG) that restrict the virus life cycle and warn the neighboring cells for the presence of the pathogen.[41] To determine whether HASQ-6Cl intensifies this antiviral signaling response, we analyzed the levels of IFNβ and the ISG IFN-induced protein with tetratricopeptide repeats 1 (IFIT1) in A549 cells upon transfection of RIG-I-CARD (a constitutively active form of RIG-I)[42–44] in the absence or presence of HASQ-6Cl. Our results demonstrate that there is no significant difference between *IFNβ* or *IFIT1* production in the presence of HASQ-6Cl (Figure 5C). In order to solidify these results, we have used the same experimental setup to analyze the activation of the signal transducer and activator of transcription 1 (STAT1, which signals IFNs produced by the neighboring cells) by western blotting using a specific antibody against the phosphorylated activated form of STAT1 (pSTAT1). As shown in Figure 5D, there are no significant differences in the amount of pSTAT1 in the presence or absence of HASQ-6Cl upon stimulation with RIG-I-CARD. Finally, to prove that HASQ-6Cl has no influence on the host immune response against IAV, we did the same analysis in the context of IAV PR8 infection, in the presence and absence of the compound. Also, in these conditions, there was no significant change in the levels of *IFNβ* and *IFIT1* mRNA (Figure 5E). These results demonstrate that there is no specific interference of HASQ-6Cl with the host immune response dependent on MAVS signaling.

Altogether, up to this point, our results indicated that HASQ-6Cl's action on physically preventing the formation of the virus-induced protein aggregates might be the real cause of the delay in virus particle formation and the consequent decrease in virus titers. These results, hence, also solidify the hypothesis that the formation of these protein aggregates is in fact stimulated by the virus, as an important part of its infection cycle.

We further characterized by mass spectrometry the insoluble fraction of A549 cells upon 8 hpi with IAV PR8, after pre-treatment with HASQ-6Cl. We first performed comparative analyses of the abundances of each viral protein in the absence or in the presence of HASQ-6Cl during infection, considering three independent replicates. This analysis demonstrates that the proteins that were previously identified as present in the insoluble fraction of IAV PR8-infected cells (NP, NS1, PB1, PB2, M1) are less abundantly present when cells are treated with HASQ-6Cl prior to infection (Figure 5F; Table S5). Afterward, to understand which host proteins were deregulated upon infection in the presence of HASQ-6Cl, we considered the proteins whose abundance ratio between IAV PR8-infected cells pre-treated with HASQ-6Cl (IAV PR8 + HASQ-6Cl) and IAV PR8-infected cells was below 0.65 with adjusted p value <0.05. A gene ontology analysis using both Cytoscape and STRING databases showed that most of the identified proteins are involved in the negative regulation of transcription and ribonucleoprotein complex biogenesis (Figure 5G; Tables S6 and S7).

These results support our previous observations that indicate that the accumulation of both viral proteins and host proteins related to the ribonucleoprotein complex biogenesis (including mRNA splicing, ribonucleoprotein complex assembly or RNA processing) in insoluble aggregates plays an important role during IAV life cycle.

To further complete this study and confirm that the effect of HASQ-6Cl on infection is due to its protein disaggregation properties, we performed similar analyses upon infection with the non-segmented negative-strand RNA virus vesicular stomatitis virus (VSV). As shown in Figure 6A, and in contrast to IAV, VSV does not induce a significant increase in the amount of insoluble proteins during infection. The

quantification of the formation of VSV infectious particles by plaque assay in the presence of HASQ-6Cl rendered no significant differences when compared to the particles produced in the absence of this compound (Figure 6B). These results hence suggest that the lack of effect of HASQ-6Cl on VSV infection is related to the absence of viral-induced protein aggregation and solidify our previous results on IAV, demonstrating that the observed accumulation of insoluble proteins is a specific characteristic of IAV infection which is essential for an efficient viral propagation.

The disruption of virus-induced aggregates inhibits the proper assembly of new influenza virions

We have further analyzed the effect of the inhibition of the formation of protein aggregates on the expression of different IAV proteins throughout the whole infectious cycle (Figure 7A). To that end, A549 cells were infected with IAV PR8 in the absence or presence of HASQ-6Cl, and the expression of IAV proteins was assessed at several times post infection by western blot.

As expected, most of the viral proteins, namely PB1, PB2, NP, are already detected after 6 hpi, while others, such as M1 and M2, are only expressed at later infection stages (Figure 7A). Except for M1 at 12 hpi, none of the viral proteins' expression was affected by the presence of HASQ-6Cl, indicating that neither the compound nor the presence of protein aggregates influences the general viral protein translation. Nevertheless, the formation of insoluble protein aggregates upon infection seems to be important for the correct expression, or at least stabilization, of M1. As M1 mediates viral assembly and budding at the plasma membrane of infected cells, by mediating the encapsidation of vRNPs into the membrane envelope,[45–47] we hypothesize that the formation of these protein aggregates is somehow favoring the final assembly of the new virus particles.

The molecular details on how IAV eight-partite genome assembles are still not well understood. However, recent data show that vRNPs associate with a modified ER,[48] to form insoluble liquid condensates, also referred as viral inclusions, at ER exit sites, through binding to the recycling endocytic marker Rab11a.[27,48–50] As infection progresses, viral inclusions augment in size. To understand whether the vesicular transport of vRNPs is being affected by the presence of HASQ-6Cl, A549 cells infected with IAV PR8, in the presence and absence of HASQ-6Cl, were stained against viral NP and host Rab11 and analyzed by immunofluorescence (Figure 7B). Rab11-positive viral inclusion areas were visualized by confocal microscopy and quantified using the ImageJ software.

The vesicles were classified into groups according to size, based on previous reports[27,50,51]: we have set four intervals comprising vesicles with a size (1) up to 0.30 μm^2, (2) 0.30–0.60 μm^2, (3) 0.60–0.90 μm^2 and (4) larger than 0.90 μm^2. The frequency distribution of viral inclusions at 8 hpi is not significantly different in the presence or in the absence of HASQ-6Cl, although at 12 hpi there is an increase in the smaller and a decrease in the larger viral inclusions, indicating HASQ-6Cl is to some extent interfering with the formation of viral inclusions and, therefore, with the final assembly of new IAV virions.

DISCUSSION

During IAV particle formation, a large amount of viral proteins is synthesized in a relatively short time, whereby protein folding can become a limiting step for their active conformation and trafficking. Proteostasis disruption, including the one triggered by viral infections, may lead to the accumulation of misfolded proteins and the induction of ER stress, activating the UPR.[52]

In this study we performed a detailed analysis of the activation and importance of each of the three (PERK-, ATF6-, and IRE1-dependent) UPR pathways in the context of a single cycle of IAV infection. This approach differs from previous studies (which, as explained above, present somewhat contradicting data), that typically investigated the relevance of the UPR in IAV infection at fewer and mostly late time points post infection (24 or 48 h post infection),[16,20] often comprising cells in diverse stages/cycles of infection. We determined that, although the levels of eIF2α phosphorylation, alongside with the expression of ATF4, GADD34, and CHOP, increase upon infection, PERK is not essential for viral propagation, as the specific PERK inhibitor GSK-2656157 had no effect on the formation of new infectious virus particles. Furthermore, IAV infection in the presence of GSK-2656157 led to a similar pattern of eIF2α phosphorylation (and consequent ATF4 and GADD34 expression) to the one observed in non-treated infected cells. eIF2α phosphorylation during IAV infection may hence result from the activation of another signaling pathway independent of PERK. The integrated stress response (ISR) combines converging stress response pathways against diverse stimuli that culminate with eIF2α phosphorylation and its downstream signaling.[53,54] Besides PERK, other kinases are implicated in the ISR, namely protein kinase R (PKR), general control nonderepressible 2 (GCN2), and heme regulated inhibitor (HRI). As PKR has been shown to be activated in response to IAV infection,[55] the observed changes are most likely due to the activation of this specific kinase. However, some IAV proteins can counteract this host defense factor,[56–58] perhaps explaining, together with the ATF4/GADD34-driven negative feedback mechanism, why we observe a transient activation of this pathway.

Although not being able to visualize the specific activation of ATF6 during a single infection cycle, using the levels of *grp78*/BiP mRNA/ protein expression as an indirect measure of ATF6 activation,[31,32] we observed no stimulation of the ATF6 UPR branch during infection. By using two different ATF6 inhibitors to study the relevance of this branch for the propagation of IAV, we were able to demonstrate that, in concert with the lack of alteration in BiP expression levels throughout the infectious cycle, the ATF6 UPR branch does not play an important role during IAV infection, as suggested in previous studies.[20,21]

The IRE1 pathway activation was observed upon infection by the increase of IRE1 phosphorylation and the splicing of the downstream factor XBP1. Inhibition of this pathway using the specific inhibitor 4µ8C results in a significant decrease in the formation of new virus particles. Our results are in agreement and complementing to those obtained by Hassan et al.,[21] where the activation of the IRE1 pathway by XBP1 splicing was observed in HTBE cells, and by Schmoldt et al.,[20] that reported that a functional IRE1 is necessary for viral NP expression. The importance of the UPR IRE1/XBP1 pathway for IAV infection is most likely due to an XBP1-dependent upregulation of genes involved
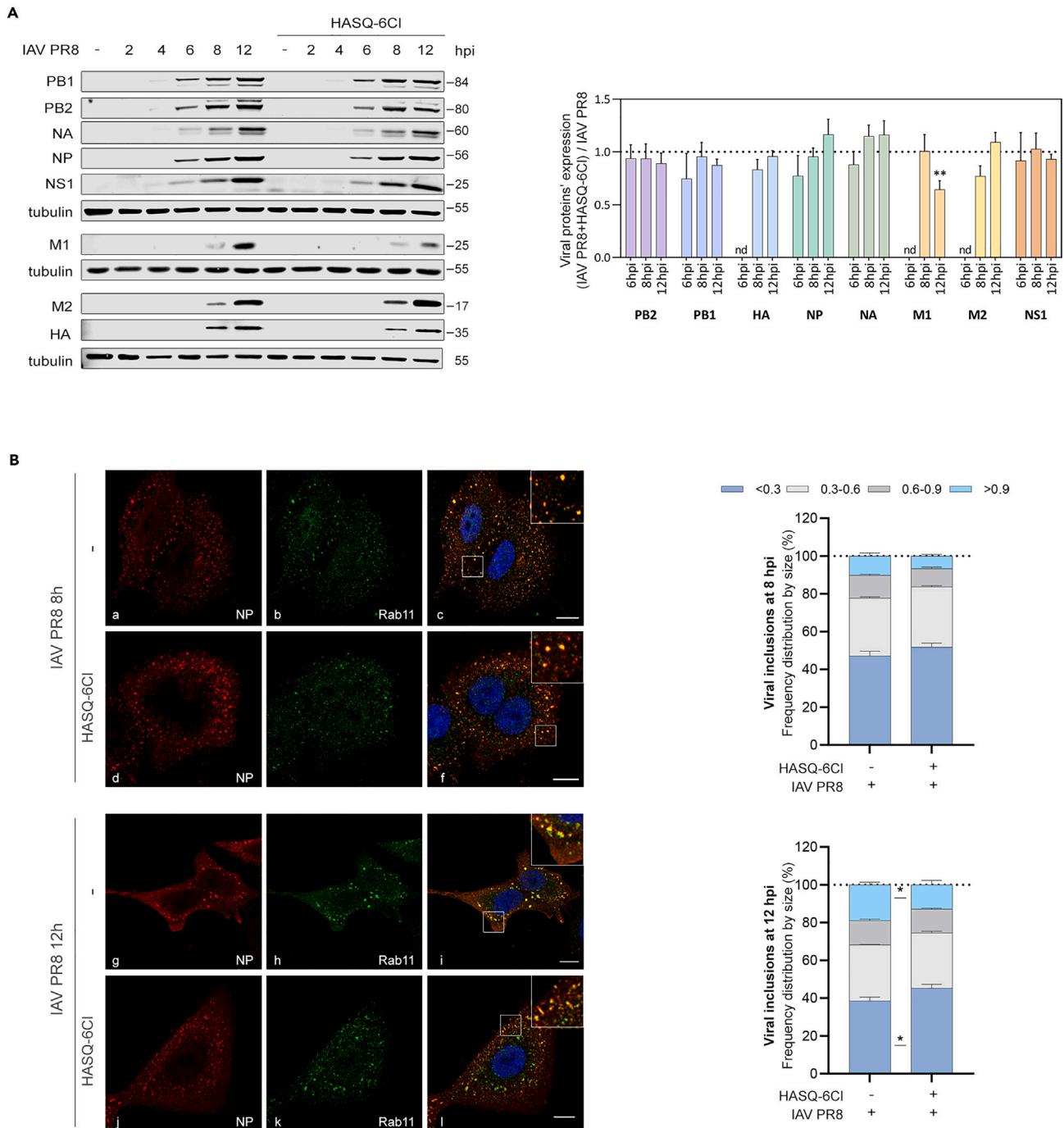
Figure 7. HASQ-6Cl interferes with viral inclusions and impedes the proper assembly of new virus particles

(A) Western blot analysis of each of the viral proteins' expression levels in IAV PR8-infected A549 cells at different times post infection, in the presence or absence of HASQ-6Cl. Tubulin was used as internal control. Quantification values were obtained after normalization to tubulin followed by the ratio between the intensity of a viral protein in an infected sample pre-treated with HASQ-6Cl (IAV PR8+HASQ-6Cl) and in an infected sample (IAV PR8), referred as (IAV PR8+HASQ-6Cl):IAV PR8. Data represents the means ± SEM of at least three independent experiments. **p < 0.001 using Student's *t* test.

(B) Characterization of the viral inclusions' size formed upon infection with IAV PR8 for 8 h or 12h in A549 cells, in the absence or in the presence of HASQ-6Cl. Confocal images of (a, d, g, j) viral NP, (b, e, h, k) Rab11 and (c, I, i, l) merge images. Bars represent 10 μm. Data represents the frequency distribution of viral inclusions by size as means ± SEM of three independent experiments, *p < 0.05 using two-way ANOVA followed by Bonferroni's multiple comparisons test. See also Tables S5–S7.

in phospholipids synthesis, chaperone expression and the activation of the ERAD machinery, that ultimately may lead to increased ER size and capacity to help viral protein folding and maturation. These results, together with the observation that the incorporation of an ER stressor such as thapsigargin during infection, restricts the expression of viral NP, reinforces the idea that IAV might benefit from low levels of ER stress possibly to facilitate the folding capacity of glycoproteins at the ER, but avoids further potentially deleterious UPR activation.[18]

The stress-induced disruption of cellular proteostasis often results in the accumulation of insoluble proteins and toxic protein aggregates, which is proposed as a transversal hallmark of several pathological conditions.[59,60] In the context of a viral infection, the accumulation of proteins into aggregates can arise from the formation of specialized sites of viral replication and assembly (generally termed viral factories) or even as part of the host cell antiviral immune response.[11,61,62] In this study we investigated whether IAV induces the accumulation of insoluble protein aggregates and disturbs the host proteostasis. Our results show that, concomitantly to a high level of viral protein translation, IAV induces an increase in the amount of the cellular insoluble protein fraction and the formation of protein aggregates, mainly at the perinuclear area. This occurs at a point of infection that coincides with the activation of the UPR IRE1 pathway and with a high viral protein translation rate, while host protein synthesis is considerably decreased.[37]

To elucidate the composition, origin and significance of the observed IAV-induced protein aggregation, we analyzed the insoluble protein fractions by LC-MS/MS. The IAV proteins NP, NS1, PB1, PB2, and M1, accumulate in the insoluble protein fraction, as well as host proteins associated to mechanisms of protein complex assembly and localization, mRNA processing and protein translation. A recent study has demonstrated that, during IAV infection, several host proteins undergo changes in solubility, and found that several viral proteins, essentially vRNP components, become strongly insoluble with infection,[63] strengthening our results.

Additionally, a previous study found several proteins belonging to the above-mentioned pathways immunoprecipitated with IAV H7N9 NP.[64] It is possible that NP recruits these proteins to enhance viral transcript translation and that they generate large insoluble complexes. Our results may also indicate that these translation related processes are deregulated upon the export of viral ribonucleoproteins from the nucleus and the viral host-shutoff to impede host proteins to be fully synthesized, which ultimately may lead to ribosome stalling and accumulation of host aberrant insoluble proteins.

To better understand the biological relevance of the accumulation of insoluble protein aggregates in the context of IAV infection, we used a tool to inhibit this aggregation, the hybrid chemical compound HASQ-6Cl (named 6c in[39]). The combination of quinolines and steroids in one single chemical entity, generates this new hybrid molecule, capable of interacting with protein aggregates through π-π (quinoline fragment), hydrophobic (steroid fragment) and hydrogen bonding interaction. Both fragments of HASQ-6Cl have important features to be able to interact with β-sheets inhibiting its consequent aggregation process. Such versatility is critical to interact with protein aggregates of yet unknown origin, such as those observed in this work. The design strategy of HASQ-6Cl followed a "framework combination" approach, avoiding the use of cleavable linkers, to retain the molecule integrity within the cellular media. Our results demonstrate that HASQ-6Cl decreases the IAV-induced protein aggregation level. Importantly, we have shown that HASQ-6Cl interferes with the virus life cycle at the viral protein production phase, which coincides with the protein aggregates formation, and consequently induces about 50% decrease in the production of infectious viral particles. This effect is likely due to the diminished formation of the virus-induced protein aggregates, as no interference of HASQ-6Cl on the splicing of XBP1, and hence on IRE1 activation, nor on the RIG-I/MAVS antiviral signaling were observed.

Mass spectrometry analysis of the insoluble fractions isolated upon IAV infection in the presence of HASQ-6Cl revealed that the viral proteins that were previously identified as present in the insoluble fraction of infected cells are less abundant in these conditions. Indeed, the presence of HASQ-6Cl during infection decreases the abundance of several viral proteins with different roles during the infection cycle, namely vRNP components (PB1, PB2, and NP), NS1 and M1, that were shown here, and by others[63] to become more insoluble upon infection with IAV PR8.

There were also changes observed at the level of the host proteins, with most of the identified proteins being involved in the negative regulation of transcription and ribonucleoprotein complex biogenesis. These results support the hypothesis that the accumulation of both viral proteins and host proteins in insoluble aggregates, or changes in its solubility, plays an important role during IAV infection. Furthermore, it suggests that HASQ-6Cl might have a multiple and broad targeting within cells to prevent the accumulation of proteins in the insoluble fraction and, therefore, restricting infection.

The proper assembly and budding of new virions require the intra-cellular transport of progeny vRNPs from the nucleus to the plasma membrane. This process is dependent on the formation of liquid viral inclusions that are hubs for the eight vRNPs close to ER exit sites, and their formation and/or transport to the plasma membrane depends on the ER-derived vesicles containing Rab11.[65–68] Recently, it was shown that nucleozin, a well-studied vRNP pharmacological modulator, can affect vRNP solubility in a Rab11-dependent manner, acting by hardening IAV inclusions to prevent efficient replication.[63] Our results show that the formation of these viral inclusions can be impacted HASQ-6Cl by decreasing their size, which is ultimately reflected in a decrease in the number of infectious IAV particles produced after a single replication cycle. Targeting this mechanism may be of particular importance as, besides being crucial for the correct assembly of every genome segment to form a fully infectious viral particle, it is also decisive for the genetic reassortment upon a co-infection of different IAV strains from distinct hosts and the emergence of novel viruses with pandemic potential.[69]

To complete our studies, and determine whether HASQ-6Cl, and its consequent inhibition of protein aggregation, affected the production of specific viral proteins, we assessed their expression at several times post infection in the absence or presence of the chemical compound. We detected no difference in the production of viral proteins in the presence of HASQ-6Cl, with the exception of M1. M1 is the most abundant protein in virions and mediates viral assembly and the budding of vRNPs at the plasma membrane of infected cells.[45,46] This protein has different roles at different stages of the infection, and it is speculated that it can change its conformational and oligomerization state

depending on its functional state.[70] One hypothetical function of the M1 oligomer is the shielding of newly synthesized vRNA/vRNPs during transport through the host cell's cytosol after nuclear export. One can then further hypothesize that the presence of HASQ-6Cl can in some extent prevent the oligomerization of M1, indirectly manipulating its function during assembly through vRNPs destabilization.

The formation of these protein aggregates and their relevance for viral propagation seems to be specific for IAV, or at least not common to all RNA viruses, as we have shown that VSV infection does not lead to an accumulation of insoluble proteins, and that the presence of HASQ-6Cl does not affect the production of infectious VSV particles.

Overall, our findings demonstrate that IAV manipulates the host cellular processes by activating the UPR and by inducing the accumulation of insoluble viral proteins and host proteins that are generally related to RNA processing. The formation of these aggregates is beneficial for the virus and seems to be required for the correct assembly of viral particles. Interfering with UPR pathways or chemically avoiding the assembly of such aggregates is sufficient to hinder viral propagation. Our results have, hence, uncovered specific IAV-host interaction mechanisms that should be further explored for the development of novel host-directed IAV antiviral therapies.

Limitations of the study

In this manuscript, we identify two independent mechanisms by which IAV manipulates host cellular proteostasis and further demonstrate that both can be chemically disrupted to prevent a productive infection. However, although we demonstrated that IAV requires the IRE1 branch of the UPR, with no effect on the PERK and ATF6 branches, the evaluation of IAV effects on ATF6 was only indirect, due to methodologic limitations.

Furthermore, even though we demonstrated that IAV can induce the accumulation of insoluble protein aggregates related mostly to host RNA metabolism, and that HASQ-6Cl can disrupt this mechanism essentially at the later stages of the infection, the exact target for this compound is not clearly identified. Lastly, our studies are limited to the PR8 strain of IAV, rather than circulating strains.

STAR★METHODS

Detailed methods are provided in the online version of this paper and include the following:

- KEY RESOURCES TABLE
- RESOURCE AVAILABILITY
  - Lead contact
  - Materials availability
  - Data and code availability
- EXPERIMENTAL MODEL AND STUDY PARTICIPANT DETAILS
  - Cell lines
  - Virus strains
- METHOD DETAILS
  - Virus stock preparation
  - Plaque assay and infection experiments
  - Unfolded protein response inhibitors
  - Experiments with the HASQ-6Cl compound
  - Plasmids and transfection
  - Immunocytochemistry and microscopy analyses
  - Isolation of the insoluble protein fraction
  - Gel electrophoresis and immunoblotting
  - RNA extraction, cDNA synthesis and quantitative real-time polymerase chain reaction
  - LC-MS/MS analyses
- QUANTIFICATION AND STATISTICAL ANALYSIS

SUPPLEMENTAL INFORMATION

Supplemental information can be found online at https://doi.org/10.1016/j.isci.2024.109100.

images and ImageJ/Fiji software. Some of the figures were created using BioRender.com. Image acquisition was performed in the LiM facility of iBiMED, a node of PPBI (Portuguese Platform of BioImaging): POCI-01-0145-FEDER-022122.

AUTHOR CONTRIBUTIONS

Conceptualization, M.M., A.R.S., and D.R.; Methodology, M.M., H.A., A.R.S., and D.R.; Investigation: M.M., B.R., M.P., D.R.R., A.N., J.S., and D.B.; Data Curation: R.V.; Writing – Original Draft: M.M, A.R.S., and D.R.; Writing – Review and Editing, M.M., A.R.F., H.A., A.S., M.J.A., A.R.S., and D.R.; Visualization, M.M.; Supervision: M.J.A., A.R.S., and D.R.; Funding Acquisition: M.J.A., A.R.S., and D.R.

DECLARATION OF INTERESTS

The authors declare no competing interests.

REFERENCES

1. Cao, S., Dhungel, P., and Yang, Z. (2017). Going against the Tide: Selective Cellular Protein Synthesis during Virally Induced Host Shutoff. J. Virol. 91, e00071-17. https://doi.org/10.1128/JVI.00071-17.

2. Levene, R.E., and Gaglia, M.M. (2018). Host Shutoff in Influenza A Virus: Many Means to an End. https://doi.org/10.3390/v10090475.

3. Marques, M., Ramos, B., Soares, A.R., and Ribeiro, D. (2019). Cellular proteostasis during influenza a virus Infection—Friend or Foe? Cells 8, 228. https://doi.org/10.3390/cells8030228.

4. Dubnikov, T., Ben-Gedalya, T., and Cohen, E. (2017). Protein quality control in health and disease. Cold Spring Harbor Perspect. Biol. 9, a023523. https://doi.org/10.1101/cshperspect.a023523.

5. Hetz, C., Zhang, K., and Kaufman, R.J. (2020). Mechanisms, regulation and functions of the unfolded protein response. Nat. Rev. Mol. Cell Biol. 21, 421–438. https://doi.org/10.1038/s41580-020-0250-z.

6. Wiseman, R.L., Mesgarzadeh, J.S., and Hendershot, L.M. (2022). Reshaping endoplasmic reticulum quality control through the unfolded protein response. Mol. Cell 82, 1477–1491. https://doi.org/10.1016/J.MOLCEL.2022.03.025.

7. Hwang, J., and Qi, L. (2018). Quality Control in the Endoplasmic Reticulum: Crosstalk between ERAD and UPR pathways. Trends Biochem. Sci. 43, 593–605. https://doi.org/10.1016/J.TIBS.2018.06.005.

8. Hartl, F.U., Bracher, A., and Hayer-hartl, M. (2011). Molecular chaperones in protein folding and proteostasis. Nature 475, 324–332. https://doi.org/10.1038/nature10317.

9. Hill, S.M., Hanzén, S., and Nyström, T. (2017). Restricted access: spatial sequestration of damaged proteins during stress and aging.

EMBO Rep. 18, 377–391. https://doi.org/10.15252/embr.201643458.

10. Netherton, C.L., and Wileman, T. (2011). Virus factories, double membrane vesicles and viroplasm generated in animal cells. Curr. Opin. Virol. 1, 381–387. https://doi.org/10.1016/j.coviro.2011.09.008.

11. Olasunkanmi, O.I., Chen, S., Mageto, J., and Zhong, Z. (2020). Virus-Induced Cytoplasmic Aggregates and Inclusions are Critical Cellular Regulatory and Antiviral Factors. Viruses 12. https://doi.org/10.3390/V12040399.

12. Taubenberger, J.K., and Morens, D.M. (2008). The Pathology of Influenza Virus Infections. Annu. Rev. Pathol. 3, 499–522. https://doi.org/10.1038/nrm2621.

13. Tekin, S., Keske, S., Alan, S., Batirel, A., Karakoc, C., Tasdelen-Fisgin, N., Simsek-Yavuz, S., Işler, B., Aydin, M., Kapmaz, M., et al. (2019). Predictors of fatality in influenza A virus subtype infections among inpatients in the 2015–2016 season. Int. J. Infect. Dis. 81, 6–9. https://doi.org/10.1016/j.ijid.2019.01.005.

14. Samji, T. (2009). Influenza A: Understanding the viral life cycle. Yale J. Biol. Med. 82, 153–159.

15. Dou, D., Revol, R., Östbye, H., Wang, H., and Daniels, R. (2018). Influenza A Virus Cell Entry, Replication, Virion Assembly and Movement. Front. Immunol. 9, 1581. https://doi.org/10.3389/FIMMU.2018.01581.

16. Roberson, E.C., Tully, J.E., Guala, A.S., Reiss, J.N., Godburn, K.E., Pociask, D.A., Alcorn, J.F., Riches, D.W.H., Dienz, O., Janssen-Heininger, Y.M.W., and Anathy, V. (2012). Influenza induces endoplasmic reticulum stress, caspase-12-dependent apoptosis, and c-Jun N-terminal kinase-mediated transforming growth factor-β release in lung epithelial cells. Am. J. Respir. Cell Mol. Biol.

46, 573–581. https://doi.org/10.1165/rcmb.2010-0460OC.

17. Landeras-Bueno, S., Fernández, Y., Falcón, A., Oliveros, J.C., and Ortín, J. (2016). Chemical genomics identifies the PERK-mediated unfolded protein stress response as a cellular target for influenza virus inhibition. mBio 7, e00085-16. https://doi.org/10.1128/mBio.00085-16.

18. Mazel-Sanchez, B., Iwaszkiewicz, J., Bonifacio, J.P.P., Silva, F., Niu, C., Strohmeier, S., Eletto, D., Krammer, F., Tan, G., Zoete, V., et al. (2021). Influenza A viruses balance ER stress with host protein synthesis shutoff. Proc. Natl. Acad. Sci. USA 118, e2024681118. https://doi.org/10.1073/PNAS.2024681118.

19. Frabutt, D.A., Wang, B., Riaz, S., Schwartz, R.C., and Zheng, Y.-H. (2018). Innate Sensing of Influenza A Virus Hemagglutinin Glycoproteins by the Host Endoplasmic Reticulum (ER) Stress Pathway Triggers a Potent Antiviral Response via ER-Associated Protein Degradation. J. Virol. 92, e01690-17. https://doi.org/10.1128/jvi.01690-17.

20. Schmoldt, C., Vazquez-Armendariz, A.I., Shalashova, I., Selvakumar, B., Bremer, C.M., Peteranderl, C., Gattenlöhner, S., Witte, B., Gattenlöhner, S., Fink, L., et al. (2019). IRE1 signaling as a putative therapeutic target in influenza virus–induced pneumonia. Am. J. Respir. Cell Mol. Biol. 61, 537–540. https://doi.org/10.1165/RCMB.2019-0123.

21. Hassan, I.H., Zhang, M.S., Powers, L.S., Shao, J.Q., Baltrusaitis, J., Rutkowski, D.T., Legge, K., and Monick, M.M. (2012). Influenza A viral replication is blocked by inhibition of the inositol-requiring enzyme 1 (IRE1) stress pathway. J. Biol. Chem. 287, 4679–4689. https://doi.org/10.1074/jbc.M111.284695.

22. Goulding, L.V., Yang, J., Jiang, Z., Zhang, H., Lea, D., Emes, R.D., Dottorini, T., Pu, J., Liu, J., and Chang, K.C. (2020). Thapsigargin at non-cytotoxic levels induces a potent host antiviral

response that blocks influenza a virus replication. Viruses *12*, 1093. https://doi.org/10.3390/v12101093.

23. Slaine, P.D., Kleer, M., Duguay, B.A., Pringle, E.S., Kadijk, E., Ying, S., Balgi, A., Roberge, M., McCormick, C., and Khaperskyy, D.A. (2021). Thiopurines Activate an Antiviral Unfolded Protein Response That Blocks Influenza A Virus Glycoprotein Accumulation. J. Virol. *95*, e00453-21. https://doi.org/10.1128/JVI.00453-21.

24. Vidic, J., Richard, C.A., Péchoux, C., Da Costa, B., Bertho, N., Mazerat, S., Delmas, B., and Chevalier, C. (2016). Amyloid assemblies of influenza a virus PB1-F2 protein damage membrane and induce cytotoxicity. J. Biol. Chem. *291*, 739–751. https://doi.org/10.1074/jbc.M115.652917.

25. Herter, S., Osterloh, P., Hilf, N., Rechtsteiner, G., Höhfeld, J., Rammensee, H.-G., and Schild, H. (2005). Dendritic Cell Aggresome-Like-Induced Structure Formation and Delayed Antigen Presentation Coincide in Influenza Virus-Infected Dendritic Cells. J. Immunol. *175*, 891–898. https://doi.org/10.4049/jimmunol.175.2.891.

26. McCormick, C., and Khaperskyy, D.A. (2017). Translation inhibition and stress granules in the antiviral immune response. Nat. Rev. Immunol. *17*, 647–660. https://doi.org/10.1038/nri.2017.63.

27. Alenquer, M., Vale-Costa, S., Etibor, T.A., Ferreira, F., Sousa, A.L., and Amorim, M.J. (2019). Influenza A virus ribonucleoproteins form liquid organelles at endoplasmic reticulum exit sites. Nat. Commun. *10*, 1629. https://doi.org/10.1038/s41467-019-09549-4.

28. De Wit, E., Spronken, M.I.J., Bestebroer, T.M., Rimmelzwaan, G.F., Osterhaus, A.D.M.E., and Fouchier, R.A.M. (2004). Efficient generation and growth of influenza virus A/PR/8/34 from eight cDNA fragments. Virus Res. *103*, 155–161. https://doi.org/10.1016/j.virusres.2004.02.028.

29. Goodman, A.G., Smith, J.A., Balachandran, S., Perwitasari, O., Proll, S.C., Thomas, M.J., Korth, M.J., Barber, G.N., Schiff, L.A., and Katze, M.G. (2007). The Cellular Protein P58IPK Regulates Influenza Virus mRNA Translation and Replication through a PKR-Mediated Mechanism. J. Virol. *81*, 2221–2230. https://doi.org/10.1128/JVI.02151-06.

30. Atkins, C., Liu, Q., Minthorn, E., Zhang, S.Y., Figueroa, D.J., Moss, K., Stanley, T.B., Sanders, B., Goetz, A., Gaul, N., et al. (2013). Characterization of a novel PERK kinase inhibitor with antitumor and antiangiogenic activity. Cancer Res. *73*, 1993–2002. https://doi.org/10.1158/0008-5472.CAN-12-3109.

31. Adachi, Y., Yamamoto, K., Okada, T., Yoshida, H., Harada, A., and Mori, K. (2008). ATF6 is a transcription factor specializing in the regulation of quality control proteins in the endoplasmic reticulum. Cell Struct. Funct. *33*, 75–89. https://doi.org/10.1247/CSF.07044.

32. Lebeau, P., Byun, J.H., Yousof, T., and Austin, R.C. (2018). Pharmacologic inhibition of S1P attenuates ATF6 expression, causes ER stress and contributes to apoptotic cell death. Toxicol. Appl. Pharmacol. *349*, 1–7. https://doi.org/10.1016/J.TAAP.2018.04.020.

33. Van Der Gucht, W., Leemans, A., De Schryver, M., Heykers, A., Caljon, G., Maes, L., Cos, P., and Delputte, P.L. (2017). Respiratory syncytial virus (RSV) entry is inhibited by serine protease inhibitor AEBSF when present during an early stage of infection. Virol. J. *14*, 157. https://doi.org/10.1186/s12985-017-0824-3.

34. Stewart, C., Estrada, A., Kim, P., Wang, D., Wei, Y., Gentile, C., and Pagliassotti, M. (2017). Regulation of IRE1α by the small molecule inhibitor 4μ8c in hepatoma cells. Endoplasmic Reticulum Stress Dis. *4*, 1–10. https://doi.org/10.1515/ersc-2017-0001.

35. Varanda, A.S., Santos, M., Soares, A.R., Vitorino, R., Oliveira, P., Oliveira, C., and Santos, M.A.S. (2020). Human cells adapt to translational errors by modulating protein synthesis rate and protein turnover. RNA Biol. *17*, 135–149. https://doi.org/10.1080/15476286.2019.1670039.

36. Pereira, M., Tomé, D., Domingues, A.S., Varanda, A.S., Paulo, C., Santos, M.A.S., and Soares, A.R. (2018). A Fluorescence-Based Sensor Assay that Monitors General Protein Aggregation in Human Cells. Biotechnol. J. *13*, e1700076. https://doi.org/10.1002/biot.201700676.

37. Bogdanow, B., Wang, X., Eichelbaum, K., Sadewasser, A., Husic, I., Paki, K., Budt, M., Hergeselle, M., Vetter, B., Hou, J., et al. (2019). The dynamic proteome of influenza A virus infection identifies M segment splicing as a host range determinant. Nat. Commun. *10*, 5518. https://doi.org/10.1038/s41467-019-13520-8.

38. Walsh, I., Seno, F., Tosatto, S.C.E., and Trovato, A. (2014). PASTA 2.0: An improved server for protein aggregation prediction. Nucleic Acids Res. *42*, W301–W307. https://doi.org/10.1093/nar/gku399.

39. Albuquerque, H.M.T., Nunes da Silva, R., Pereira, M., Maia, A., Guieu, S., Soares, A.R., Santos, C.M.M., Vieira, S.I., and Silva, A.M.S. (2022). Steroid-Quinoline Hybrids for Disruption and Reversion of Protein Aggregation Processes. ACS Med. Chem. Lett. *13*, 443–448. https://doi.org/10.1021/acsmedchemlett.1c00604.

40. Steinberg, J., Wadenpohl, T., and Jung, S. (2021). The endogenous RIG-I ligand is generated in influenza a-virus infected cells. Viruses *13*, 1564. https://doi.org/10.3390/v13081564.

41. Thoresen, D., Wang, W., Galls, D., Guo, R., Xu, L., and Pyle, A.M. (2021). The molecular mechanism of RIG-I activation and signaling. Immunol. Rev. *304*, 154–168. https://doi.org/10.1111/IMR.13022.

42. Ferreira, A.R., Gouveia, A., Magalhães, A.C., Valença, I., Marques, M., Kagan, J.C., and Ribeiro, D. (2022). Human Cytomegalovirus vMIA Inhibits MAVS Oligomerization at Peroxisomes in an MFF-Dependent Manner. Front. Cell Dev. Biol. *10*, 871977. https://doi.org/10.3389/fcell.2022.871977.

43. Ferreira, A.R., Magalhães, A.C., Camões, F., Gouveia, A., Vieira, M., Kagan, J.C., and Ribeiro, D. (2016). Hepatitis C virus NS3-4A inhibits the peroxisomal MAVS-dependent antiviral signalling response. J. Cell Mol. Med. *20*, 750–757. https://doi.org/10.1111/jcmm.12801.

44. Magalhães, A.C., Ferreira, A.R., Gomes, S., Vieira, M., Gouveia, A., Valença, I., Islinger, M., Nascimento, R., Schrader, M., Kagan, J.C., and Ribeiro, D. (2016). Peroxisomes are platforms for cytomegalovirus' evasion from the cellular immune response. Sci. Rep. *6*, 26028. https://doi.org/10.1038/srep26028.

45. Dahmani, I., Ludwig, K., and Chiantia, S. (2019). Influenza A matrix protein M1 induces lipid membrane deformation via protein multimerization. Biosci. Rep. *39*. https://doi.org/10.1042/BSR20191024.

46. Kordyukova, L.V., Shtykova, E.V., Baratova, L.A., Svergun, D.I., and Batishchev, O.V. (2019). Matrix proteins of enveloped viruses: a case study of Influenza A virus M1 protein. J. Biomol. Struct. Dyn. *37*, 671–690. https://doi.org/10.1080/07391102.2018.1436089.

47. Gao, Q., Chou, Y.-Y., Doğanay, S., Vafabakhsh, R., Ha, T., and Palese, P. (2012). The Influenza A Virus PB2, PA, NP, and M Segments Play a Pivotal Role during Genome Packaging. J. Virol. *86*, 7043–7051. https://doi.org/10.1128/jvi.00662-12.

48. De Castro Martin, I.F., Fournier, G., Sachse, M., Pizarro-Cerda, J., Risco, C., and Naffakh, N. (2017). Influenza virus genome reaches the plasma membrane via a modified endoplasmic reticulum and Rab11-dependent vesicles. Nat. Commun. *8*, 1396–1412. https://doi.org/10.1038/s41467-017-01557-6.

49. Vale-Costa, S., and Amorim, M.J. (2017). Clustering of Rab11 vesicles in influenza A virus infected cells creates hotspots containing the 8 viral ribonucleoproteins. Small GTPases *8*, 71–77. https://doi.org/10.1080/21541248.2016.1199190.

50. Vale-Costa, S., Alenquer, M., Sousa, A.L., Kellen, B., Ramalho, J., Tranfield, E.M., and Amorim, M.J. (2016). Influenza A virus ribonucleoproteins modulate host cell recycling by competing with Rab11 effectors. J. Cell Sci. *129*, 1697–1710. https://doi.org/10.1242/jcs.188409.

51. Möbius, W., van Donselaar, E., Ohno-Iwashita, Y., Shimada, Y., Heijnen, H.F.G., Slot, J.W., and Geuze, H.J. (2003). Recycling compartments and the internal vesicles of multivesicular bodies harbor most of the cholesterol found in the endocytic pathway. Traffic *4*, 222–231. https://doi.org/10.1034/j.1600-0854.2003.00072.x.

52. Li, S., Kong, L., and Yu, X. (2015). The expanding roles of endoplasmic reticulum stress in virus replication and pathogenesis. Crit. Rev. Microbiol. *41*, 150–164. https://doi.org/10.3109/1040841X.2013.813899.

53. Donnelly, N., Gorman, A.M., Gupta, S., and Samali, A. (2013). The eIF2α kinases: their structures and functions. Cell. Mol. Life Sci. *70*, 3493–3511. https://doi.org/10.1007/S00018-012-1252-6.

54. Pakos-Zebrucka, K., Koryga, I., Mnich, K., Ljujic, M., Samali, A., and Gorman, A.M. (2016). The integrated stress response. EMBO Rep. *17*, 1374–1395. https://doi.org/10.15252/EMBR.201642195.

55. Katze, M.G., Tomita, J., Black, T., Krug, R.M., Safer, B., and Hovanessian, A. (1988). Influenza virus regulates protein synthesis during infection by repressing autophosphorylation and activity of the cellular 68,000-Mr protein kinase. J. Virol. *62*, 3710–3717. https://doi.org/10.1128/JVI.62.10.3710-3717.1988.

56. Min, J.Y., Li, S., Sen, G.C., and Krug, R.M. (2007). A site on the influenza A virus NS1 protein mediates both inhibition of PKR activation and temporal regulation of viral RNA synthesis. Virology *363*, 236–243. https://doi.org/10.1016/j.virol.2007.01.038.

57. Guan, Z., Liu, D., Mi, S., Zhang, J., Ye, Q., Wang, M., Gao, G.F., and Yan, J. (2010). Interaction of Hsp40 with influenza virus M2 protein: Implications for PKR signaling pathway. Protein Cell *1*, 944–955. https://doi.org/10.1007/s13238-010-0115-x.

58. Sharma, K., Tripathi, S., Ranjan, P., Kumar, P., Garten, R., Deyde, V., Katz, J.M., Cox, N.J., Lal, R.B., Sambhara, S., and Lal, S.K. (2011).

Influenza a virus nucleoprotein exploits Hsp40 to inhibit PKR activation. PLoS One 6, e20215. https://doi.org/10.1371/journal.pone.0020215.

59. Hipp, M.S., Kasturi, P., and Hartl, F.U. (2019). The proteostasis network and its decline in ageing. Nat. Rev. Mol. Cell Biol. 20, 421–435. https://doi.org/10.1038/s41580-019-0101-y.

60. Tyedmers, J., Mogk, A., and Bukau, B. (2010). Cellular strategies for controlling protein aggregation. Nat. Rev. Mol. Cell Biol. 11, 777–788. https://doi.org/10.1038/nrm2993.

61. Moshe, A., and Gorovits, R. (2012). Virus-Induced Aggregates in Infected Cells. Viruses 4, 2218–2232. https://doi.org/10.3390/v4102218.

62. Wileman, T. (2007). Aggresomes and Pericentriolar Sites of Virus Assembly: Cellular Defense or Viral Design? Annu. Rev. Microbiol. 61, 149–167. https://doi.org/10.1146/annurev.micro.57.030502.090836.

63. Etibor, T.A., Vale-Costa, S., Sridharan, S., Brás, D., Becher, I., Mello, V.H., Ferreira, F., Alenquer, M., Savitski, M.M., and Amorim, M.-J. (2023). Defining basic rules for hardening influenza A virus liquid condensates. Elife 12, e85182. https://doi.org/10.7554/ELIFE.85182.

64. Sun, N., Sun, W., Li, S., Yang, J., and Yang, L. (2015). Proteomics Analysis of Cellular Proteins Co-Immunoprecipitated with Nucleoprotein of Influenza A Virus (H7N9). Int. J. Mol. Sci. 16, 25982–25998. https://doi.org/10.3390/ijms161125934.

65. Amorim, M.J., Bruce, E.A., Read, E.K.C., Foeglein, Á., Mahen, R., Stuart, A.D., and Digard, P. (2011). A Rab11- and Microtubule-Dependent Mechanism for Cytoplasmic Transport of Influenza A Virus Viral RNA. J. Virol. 85, 4143–4156. https://doi.org/10.1128/JVI.02606-10.

66. Eisfeld, A.J., Kawakami, E., Watanabe, T., Neumann, G., and Kawaoka, Y. (2011). RAB11A Is Essential for Transport of the Influenza Virus Genome to the Plasma Membrane. J. Virol. 85, 6117–6126. https://doi.org/10.1128/JVI.00378-11.

67. Han, J., Ganti, K., Sali, V.K., Twigg, C., Zhang, Y., Manivasagam, S., Liang, C.Y., Vogel, O.A., Huang, I., Emmanuel, S.N., et al. (2021). Host factor Rab11a is critical for efficient assembly of influenza A virus genomic segments. PLoS Pathog. 17, e1009517. https://doi.org/10.1371/journal.ppat.1009517.

68. Amorim, M.J. (2018). A comprehensive review on the interaction between the host GTPase Rab11 and influenza A virus. Front. Cell Dev. Biol. 6, 176. https://doi.org/10.3389/FCELL.2018.00176/BIBTEX.

69. Nturibi, E., Bhagwat, A.R., Coburn, S., Myerburg, M.M., and Lakdawala, S.S. (2017). Intracellular Colocalization of Influenza Viral RNA and Rab11A Is Dependent upon Microtubule Filaments. J. Virol. 91, e01179-17. https://doi.org/10.1128/JVI.01179-17.

70. Peukes, J., Xiong, X., and Briggs, J.A.G. (2021). New Structural Insights into the Multifunctional Influenza A Matrix Protein 1 (Preprint at John Wiley & Sons, Ltd). https://doi.org/10.1002/1873-3468.14194.

71. Ernandes, M.J., and Kagan, J.C. (2021). Interferon-Independent Restriction of RNA Virus Entry and Replication by a Class of Damage-Associated Molecular Patterns. mBio 12, e00584-21. https://doi.org/10.1128/MBIO.00584-21.

STAR★METHODS

KEY RESOURCES TABLE

REAGENT or RESOURCE	SOURCE	IDENTIFIER
Antibodies		
Mouse monoclonal anti-influenza A virus nucleoprotein [AA5H]	Abcam	Cat# ab20343; RRID: AB_445525
Mouse monoclonal anti-influenza A virus hemagglutinin (C102)	Santa Cruz Biotechnology	Cat# sc-52025; RRID: AB_629813
Rabbit monoclonal anti-influenza A virus neuraminidase [HL1108]	GeneTex	Cat# GTX636323; RRID: AB_2909968
Mouse monoclonal anti-influenza A virus M1 (FluAc)	Santa Cruz Biotechnology	Cat# sc-69824; RRID: AB_1124287
Mouse monoclonal anti-influenza A virus M2 (14C2)	Santa Cruz Biotechnology	Cat# sc-32238; RRID: AB_627808
Rabbit polyclonal anti-influenza A virus NP	Alenquer et al.[27]	N/A
Rabbit polyclonal anti-influenza A virus PB1	Alenquer et al.[27]	N/A
Rabbit polyclonal anti-influenza A virus PB2	Alenquer et al.[27]	N/A
Rabbit polyclonal anti-influenza A virus NS1	Alenquer et al.[27]	N/A
Mouse monoclonal anti-Rab11	Santa Cruz Biotechnology	Cat# sc-166912; RRID: AB_10611645
Rabbit recombinant monoclonal anti-IRE1 (14C10)	Cell Signaling Technology	Cat# 3294; RRID: AB_82354594
Rabbit polyclonal anti-IRE1 (phospho S724)	Abcam	Cat# ab48187; RRID:AB_873899
Mouse monoclonal anti-CHOP (L63F7)	Cell Signaling Technology	Cat# 2895; RRID: AB_2089254
Mouse monoclonal anti-eIF2α (D-3)	Santa Cruz Biotechnology	Cat# sc-133132; RRID: AB_1562699
Rabbit monoclonal anti-phospho-eIF2α (S1)	Abcam	Cat# ab32157; RRID: AB_732117
Rabbit polyclonal anti-ATF4 (R239)	Bioworld Technology	Cat# BS1026; RRID: AB_1662053
Rabbit polyclonal anti-GADD34	Thermo Fisher Scientific	Cat# PA5-30486; RRID: AB_2547960
Rabbit recombinant monoclonal anti-PERK (C33E10)	Cell Signaling Technology	Cat# 3192; RRID: AB_2095847
Mouse monoclonal anti-BiP	BD Biosciences	Cat# 610978; RRID: AB_398291
Rabbit monoclonal anti-phospho STAT1 (Y701)	Cell Signaling	Cat# 9167; RRID: AB_561284
Mouse monoclonal anti-α-Tubulin	Sigma-Aldrich	Cat# T9026; RRID: AB_477593
Donkey polyclonal anti-Rabbit IgG (H+L) Alexa Fluor™ 488	Thermo Fisher Scientific	Cat# A-21206; RRID: AB_2535792
Donkey polyclonal anti-Mouse IgG (H+L) Alexa Fluor™ 488	Thermo Fisher Scientific	Cat# A-21202; RRID: AB_141607
Donkey polyclonal anti-Mouse IgG (H+L) Alexa Fluor™ 647	Thermo Fisher Scientific	Cat# A-31571; RRID: AB_162542
Donkey polyclonal anti-Rabbit IgG (H+L) TRITC	Jackson ImmunoResearch	Cat# 711-025-152; RRID: AB_2340588
Goat polyclonal anti-Rabbit IgG (H+L) IRDye 800CW	LI-COR Biosciences	Cat# 926-32211; RRID: AB_621843
Goat polyclonal anti-Mouse IgG (H+L) IRDye 680RD	LI-COR Biosciences	Cat# 926-68070; RRID: AB_10956588
Goat polyclonal anti-Mouse IgG (H+L) HRP conjugate	Bio-Rad	Cat# 1706516; RRID: AB_2921252
Goat polyclonal anti-Rabbit IgG (H+L) HRP conjugate	Bio-Rad	Cat# 1706515; RRID: AB_11125142
Bacterial and virus strains		
Influenza A/Puerto Rico/8/34 (H1N1) (PR8)	Wit et al.[28]	N/A
Vesicular stomatitis virus (VSV) Indiana strain	Ernandes et al.[71]	N/A
Chemicals, peptides, and recombinant proteins		
PERK inhibitor GSK-2656157	VWR International	Cat# BIOV9466-5; CAS: 1337532-29-2
IRE1 inhibitor 4μ8C	Calbiochem	Cat# 412512; CAS: 14003-96-4

(Continued on next page)

Continued

REAGENT or RESOURCE	SOURCE	IDENTIFIER
AEBSF	Tocris Bioscience	Cat# 5175; CAS: 30827-99-7
SP1 inhibitor PF-429242 dihydrochloride	Tocris Bioscience	Cat# 3354; CAS: 2248666-66-0
HASQ-6Cl	Albuquerque et al.[39]	N/A
BlueSafe	NZYTech	Cat# MB15201
DMEM, high glucose, pyruvate, no glutamine	ThermoFisher	Cat# 21969035
L-Glutamine	ThermoFisher	Cat# 25030081
Penicillin-Streptomycin Solution	ThermoFisher	Cat# 15070063
Fetal Bovine Serum	ThermoFisher	Cat# 10270106
Triton X-100	Merk Millipore	Cat# T8787
NP-40	MP Biomedicals	Cat# 11481924
Critical commercial assays		
Proteostat Aggresome Detection Kit	Enzo Life Sciences	Cat# ENZ-51038
Lipofectamine™ 3000 Transfection Reagent	Invitrogen	Cat# L3000008
Deposited data		
Raw and analyzed proteomics data	This paper	PRIDE: PXD043310
Experimental models: Cell lines		
A549	ATCC	Cat# CCL-185
HeLa HSPB1:GFP	Pereira et al.[36]	N/A
HEK293T	ATCC	Cat# CRL-3216
MDCK	ATCC	Cat# CRL-2935
Vero	Kindly given by Sílvia Correia	Cat# CCL-81
Oligonucleotides		
Primers for human *XBP1*: Forward: 5'-TTACGAGAGAAAACTCATGGCC-3' and Reverse: 5'-GGGTCCAAGTTGTCCAGAATGC-3'	This paper	N/A
Primers for human *XBP1* spliced: Forward: 5'- CTGAGTCCGAATCAGGTGCAG-3' and Reverse: 5'-ATCCATGGGGAGATGTTCTGG-3'	This paper	N/A
Primers for human *IFN-β*: Forward: 5'-TGGCACAACAGGTAGTAGGC-3' and Reverse: 5'-TGGAGAAGCACAACAGGAGAG-3'	This paper	N/A
Primers for human *GAPDH*: Forward: 5'-AAGGTGAAGGTCGGAGTC-3' and Reverse: 5'-GGGTGGAATCATATTGGAACAT-3'	This paper	N/A
Primers for human *ATF4*: Forward: 5'-AGATAGGAAGCCAGACTA-3' and Reverse: 5'-CTCATACAGATGCCACTA-3'	This paper	N/A
Primers for human *GRP78*: Forward: 5'-TTACTTAGATTGTGTTCCT-3' and Reverse: 5'- TCTCTATCTCTTGACCTT-3'	This paper	N/A
Recombinant DNA		
GFP-RIG-I-CARD	Kindly given by Friedemann Weber	N/A
Software and algorithms		
Image Studio™ Lite Software 5.2.5	LI-COR Biosciences	https://www.licor.com/bio/image-studio-lite/; RRID: SCR_013715
GraphPad Prism 9	GraphPad Software Inc	https://www.graphpad.com/; RRID: SCR_002798

(Continued on next page)

Continued

REAGENT or RESOURCE	SOURCE	IDENTIFIER
Proteome Discoverer 2.4.0.305	Thermo Fisher Scientific	https://www.thermofisher.com/pt/en/home/industrial/mass-spectrometry/liquid-chromatography-mass-spectrometry-lc-ms/lc-ms-software/multi-omics-data-analysis/proteome-discoverer-software.html; RRID: SCR_014477
ZEN Microscopy Software 3.3	Carl Zeiss	https://www.zeiss.com/microscopy/en/products/software/zeiss-zen.html; RRID: SCR_013672
Fiji/ImageJ	National Institute of Health	http://fiji.sc; RRID: SCR_002285
STRING	STRING Consortium	http://string.embl.de/; RRID: SCR_005223
Cytoscape 3.8.2	Cytoscape Consortium	http://cytoscape.org; RRID: SCR_003032
BioRender	BioRender	http://biorender.com; RRID: SCR_018361

RESOURCE AVAILABILITY

Lead contact

Further information and inquiries should be directed to and will be fulfilled by the lead contact, Daniela Ribeiro (daniela.ribeiro@ua.pt).

Materials availability

This study did not generate new unique reagents.

Data and code availability

- The mass spectrometry proteomics data have been deposited to the ProteomeXchange Consortium via the PRIDE partner repository and are publicly available as of the date of publication. Accession numbers are listed in the key resources table.
- This paper does not report original code.
- Any additional information required to reanalyze the data reported in this paper is available from the lead contact on request.

EXPERIMENTAL MODEL AND STUDY PARTICIPANT DETAILS

Cell lines

Human lung epithelial cells (A549, ATCC (CCL-185)), human embryonic kidney cells (HEK293T, ATCC (CRL-3216)) and Mardin-Darby Canine Kidney (MDCK, ATCC (CRL-2935)) were A549s and MDCKs were obtained from Prof. Paul Digard, Roslin Institute, UK, as part of collaborative work. Vero cells (isolated from kidney epithelial cells from an African green monkey, ATCC (CCL-81) were kindly provided by Dr Sílvia Correia. HeLa cells expressing a HSPB1:GFP reporter (HeLa HSPB1:GFP) cells were produced in-house and characterized in.[36] A549 and HeLa HSPB1:GFP were used as models to perform the infections with influenza A virus and/or vesicular stomatitis virus. HEK293T, MDCK and Vero were used to propagate and titrate virus, but not the subject of the study themselves. Cells were routinely tested for mycoplasma contamination and tested negative. Cells were cultured in Dulbecco's modified Eagle's medium (DMEM) high glucose (4,5 g/L) supplemented with 10% fetal bovine serum (FBS) and 100U/mL of penicillin and 100 mg/mL streptomycin and maintained at 37°C in a humidified atmosphere containing 5% v/v CO_2.

Virus strains

Influenza A/Puerto Rico/8/34 (IAV PR8; H1N1) was rescued from HEK293T cells by reverse-genetics and titrated by plaque assay in MDCK cells. Vesicular stomatitis virus (VSV) Indiana strain parental stock was kindly provided by Dr. Jonathan Kagan (Boston Children's Hospital, Harvard Medical School), and viruses were propagated and titrated in Vero cells.

METHOD DETAILS

Virus stock preparation

Reverse-genetics engineered influenza A/Puerto Rico/8/34 (IAV PR8; H1N1) were rescued in HEK293T cells using a pDUAL plasmid system. This virus was produced upon transfection of eight plasmids encoding the gene segments of IAV PR8 using PEI transfection reagent in DMEM high glucose (4.5 g/L) with pyruvate (0.11 g/L), supplemented with glutamine, without FBS or antibiotics. 24 h post transfection, the medium was changed to 2 mL of serum-free media (SFM) supplemented with 1% P/S, with 0.14% BSA and 1 μg/mL trypsin-TPCK. After two days of incubation under the same growing conditions, the supernatant was collected (P0) and centrifuged at 3000 rpm for 5 min. Clarified

supernatant with low number of viruses was stored at -80°C and further quantified by plaque assay. To prepare virus stocks, MDCK cells were infected with P0 aliquots in SFM supplemented with 0.14% BSA and 1 µg/mL trypsin-TPCK, with a MOI of 0.01. After virus adsorption for one hour, cells were cultured for two days at 37°C, 5% CO2. After centrifugation for 5 min at 3000 rpm, clarified supernatants were aliquoted and stored at -80°C. Virus stock or samples titers were determined by plaque assay.

VSV were propagated in highly confluent Vero cells, using a MOI of 0.001. The virus inoculum was diluted in SFM and after virus adsorption for one hour, an incubation of 18 h ensued. A centrifugation for 5 min at 500 g, 4°C was carried out to collect the clarified supernatant. Then, an ultracentrifugation of the supernatant for 90 min at 24000 rpm, 4°C followed and, once the supernatant was discarded, 0.35 mL of NTE buffer (0.1M NaCl, 1mM EDTA, 0.1M Tris pH 7.4) was added and incubated on ice, overnight. The next day, 4 mL of sucrose 10% NTE (ice-cold) was overlayed with 1 mL of virus suspension and ultracentrifuged for 60 min at 40500 rpm, 4°C. The supernatant was removed, and the pellet was incubated with 0.5 mL of NTE buffer on Ice, overnight. Finally, the virus suspension was aliquoted and stored at -80°C. Virus stock or samples titers were determined by plaque assay.

Plaque assay and infection experiments

To quantify IAV, MDCK cells were cultured with 10-fold dilutions of virus suspension and allowed to absorb for 1h. Cells were then cultured in 50% avicel-containing SFM supplemented with 0.14% BSA and 1 µg/mL trypsin-TPCK for 1.5 to 2 days. Cellular monolayers were fixed in 4% paraformaldehyde and stained with 0.1% toluidine blue. To quantify VSV, Vero cells were used and the avicel-containing SFM media were in this case supplemented with 1% FBS and the protocol ran for 1 day.

To perform infection, A549 cells were seeded to achieve a confluency of 80% at the time of the infection. The day after, cells were washed with PBS and infected with IAV PR8 or VSV at a MOI of 3, prepared in SFM. After one hour, cells were overlaid with DMEM supplemented with 20% FBS and 1% P/S and incubated for the desired times at 37°C in 5% CO2. In the case of samples used to determine viral production, cells were infected and after 1 h incubation, the supernatant was removed, cells were rinsed with acid wash buffer 1x (135 mM NaCl, 10 mM KCl, 40 mM citric acid, pH 3), washed in PBS and incubated in SFM supplemented with 0.14% BSA, and 1 µg/mL trypsin-TPCK (for IAV only), for up to 16 hpi.

Unfolded protein response inhibitors

UPR inhibitors (see key resources table) were added to the cells, at the indicated concentrations, 1 h prior to infection. Different concentrations of each inhibitor were tested to check for cell viability to define which one to use. The number of the infectious particles formed were normalized to the cell viability in each condition.

Experiments with the HASQ-6Cl compound

The HASQ-6Cl compound was solubilized in 100% ethanol (EtOH) to obtain a stock concentration of 100 mM. The cytotoxicity of HASQ-6Cl and EtOH was assessed by MTT cell viability assay. To do that, cells were seeded into a 96-well plate at a density of 8x103 cells/plate and allowed to adhere for 24 h at growing conditions. The day after, cells were treated with various concentrations of the compound (100, 50, 25 and 10 µM) or the correspondent EtOH percentage (1, 0.5, 0.25 and 0.1%) and incubated for 30 h at 37°C in a CO2 incubator. Compound-containing solutions were sterilized using a 0.2 µm filter. Cells were then washed twice with PBS and incubated to DMEM with 10% MTT (working solution 5 mg/mL in phosphate buffer) for 2 h at growing conditions. Lastly, this medium was removed, and the formazan crystals formed were solubilized using DMSO for 10 min at room temperature and the intensity was quantified at 575 nm. Untreated cells were used as control and the blank value was subtracted to all conditions. Further experiments were performed using 50 µM of HASQ-6Cl. The compound was added to the cells 12h before infection.

Plasmids and transfection

A549 cells were transfected with GFP-RIG-I-CARD by 10h incubation with Lipofectamine™ 3000 Transfection Reagent (Invitrogen) according to manufacturers' protocol.

Immunocytochemistry and microscopy analyses

Cells grown in 12ømm glass coverslips were fixated for 20 min with 4% paraformaldehyde in PBS, pH 7.4, followed by permeabilization with 0.2% triton X-100 for 10 min, blocking with 1% BSA for 10 min, and immunostaining with the indicated primary and secondary antibody for 1 h each. This procedure was done at room temperature, with cells being washed three times between each step. Primary antibodies and the fluorophores used are listed in the key resources table. When needed, staining with Proteostat Aggresome Dectetion kit (Enzo Life Sciences International) was performed for 30 min. Cells were additionally incubated with Hoechst dye for 2 min before being mounted in slides, using Mowiol 4-88 (AppliChem Inc.) containing propyl gallate (Sigma-Aldrich). Confocal images were acquired using a Zeiss LSM 880 confocal microscope (Carl Zeiss) and a Plan-Apochromat 63× and 100×/1.4 NA oil objectives, a 561 nm DPSS laser and the argon laser line 488 nm (BP 505–550 and 595–750 nm filters).

All images chosen are representative of at least three independent experiments and further processing or quantifications were done using ZEN Blue (Carl Zeiss) or Fiji (NIH) software. Quantification of the NP intensity in PR8-infected A549 cells was performed after sketching the region of interest (ROI) of the nucleus of each cell and obtaining the correspondent intensity mean gray value using the Zeiss Blue Software

for image processing (Carl Zeiss). Characterization of viral inclusions, positive for Rab11, by size in infected cells was performed using Fiji/ImageJ software (NIH). The vesicles were divided into groups according to size, based on previous reports.[27,49,52] In uninfected cells, the areas for viral inclusions are consistent with values <0.15 μm^2.[52] With infection, the frequency distribution from inclusions measuring 0.15-0.30 μm^2 and bigger than 0.3 μm^2 augmented significantly in relation to non-infected cells.[50] As we propose to compare the areas in infected cells only, we have set four intervals comprising viral inclusions with a size (1) up to 0.30 μm^2, (2) 0.30-0.60 μm^2, (3) 0.60-0.90 μm^2 and (4) larger than 0.90 μm^2.

Isolation of the insoluble protein fraction

To obtain total protein extracts, cell pellets were resuspended in Empigen Lysis Buffer (ELB) (0.5% Triton X-100, 50 mM HEPES, 250 mM NaCl, 1 mM DTT, 1 mM NaF, 2 mM EDTA, 1 mM EGTA, 1 mM PMSF, 1 mM Na$_3$VO$_4$ supplemented with a cocktail of protease inhibitors). Protein extracts were then sonicated, and centrifuged 20 min at 200 g at 4°C. In the end, supernatants were kept for the next phase of total protein quantification. During all procedures, cells remained on ice to avoid the activity of proteases. Quantification of total protein was performed using Pierce™ Bovine Serum Albumin Protein Assay Kit (Thermo Scientific), following the manufacturer's instructions.

To isolate the insoluble protein fraction, 100 μg of total protein was diluted in ELB to reach a final volume of 100 μL. Samples were centrifuged for 16,000 g, 20 min at 4°C to obtain the insoluble fraction. The resulting pellet was solubilized in ELB supplemented with 20% NP-40 (10%). Samples were sonicated for three cycles of five seconds (0.5 cycles with amplitude at 50-60%). After sonication cycles, samples underwent another centrifugation round (16,000 g, 20 min at 4°C). The supernatant was removed, the pellet was resuspended in ELB, and after adding the loading buffer, samples were denatured at 95°C for 5 min and run into an SDS-PAGE. In parallel, 10 μg of total protein extracts were run as loading controls. Finally, the gel was stained with BlueSafe (NZYTech) solution for at least 30 min and, after destained with distilled water, gels were scanned using Odyssey Infrared Imaging System (LI-COR Biosciences). The relative amount of insoluble protein for each sample was calculated by dividing the intensities of the insoluble protein extracts by the intensities of the corresponding total protein extracts.

Gel electrophoresis and immunoblotting

Cells were pelleted and washed before being resuspended in ELB supplemented with protease-inhibitors mix. Samples were then incubated on a rotary mixer for 15 min at 4°C and, after sonication using Clifton SW3H 38kHz bath (5 cycles 30 s on; 30 s off), the incubation was repeated. After clearing by centrifugation (17000 g, 15 min at 4°C, the supernatant was collected, and protein concentration was determined using Pierce™ Bovine Serum Albumin (BCA) Protein Assay Kit (Thermo Scientific) . Protein samples were separated by SDS-PAGE on 10 or 12.5% polyacrylamide gels, alongside with a pre-stained protein marker (GRS Protein Marker Multicolour Tris-Glicine 4∼20%, Grisp), wet transferred to nitrocellulose (PROTAN®), and analyzed by immunoblotting.

Immunoblots were processed using specific primary and secondary antibodies (see key resources table). For quantification, immunoblots were scanned with Odyssey CLx (LI-COR Biosciences) or with ChemiDoc Imaging System (BioRad), and processed using the volume tools from Image Studio Lite Ver 5.2 software (LI-COR Biosciences).

RNA extraction, cDNA synthesis and quantitative real-time polymerase chain reaction

Total RNA was isolated using NZYol reagent according to manufacturer's instructions and quantified using DS-11 spectrophotometer (DeNovix Inc.), cDNA synthesis was obtained using 0.5 to 1 μg RNA, after a pre-treatment with DNAse (Thermo Scientific), using Revert Aid Reverse Transcriptase (Thermo Scientific) and Oligo-dT15 primer (Eurofins Genomics) following manufacturer's protocol.

When needed, primer sequences were designed using Beacon Designer 7 (Premier Biosoft). The oligonucleotides used are listed in the key resources table. *GAPDH* was used as a reference gene. RT-qPCR was performed in duplicate using 2x SYBR Green qPCR Master Mix (Low Rox) (Bimake), cDNA samples were diluted 1:10 and the concentration of each primer was 250 nM, with the exception for IFN-β in which we use undiluted samples and a primer concentration of 500 nM. Reactions were run on Applied Biosystems 7500 Real Time PCR System (Applied Biosystems). The thermocycling reaction was done by heating at 95°C during 3 min, followed by 40 cycles of a 12 s denaturation step at 95°C and a 30 s annealing/elongation step at 60°C. The fluorescence was measured after the extension step using the Applied Biosystems software (Applied Biosystems). After the thermocycling reaction, the melting step was performed with slow heating, starting at 60°C and with a rate of 1%, up to 95°C, with continuous measurement of fluorescence. Data analysis was performed using the quantitative $2-\Delta\Delta CT$ method.

LC-MS/MS analyses

Samples were processed for proteomics analysis by the proteomics facility at i3S - Instituto de Investigação e Inovação em Saúde, Porto, Portugal. Briefly, the enzymatic digestion was performed with Trypsin/LysC (2 μg) overnight at 37°C at 1000 rpm. Protein identification and quantitation was performed by nanoLC-MS/MS. This equipment is composed by an Ultimate 3000 liquid chromatography system coupled to a Q-Exactive Hybrid Quadrupole-Orbitrap mass spectrometer (Thermo Scientific). Samples were loaded onto a trapping cartridge (Acclaim PepMap C18 100Å, 5 mm x 300 μm i.d., 160454, Thermo Scientific) in a mobile phase of 2% I, 0.1% FA at 10 μL/min. After 3 min loading, the trap column was switched in-line to a 50 cm by 75μm inner diameter EASY-Spray column (ES803, PepMap RSLC, C18, 2 μm, Thermo Scientific, Bremen, Germany) at 300 nL/min. Separation was generated by mixing A: 0.1% FA, and B: 80% I, with the following gradient for total protein fraction: 5 min (2.5% B to 10% B), 120 min (10% B to 30% B), 20 min (30% B to 50% B), 5 min (50% B to 99% B) and 10 min (hold 99% B). Subsequently, the column was equilibrated with 2.5% B for 17 min and a specific gradient for the Insoluble fractions: 5 min (2.5% B to

10% B), 30 min (10% B to 30% B), 50 min (30% B to 50% B), 45 min (50% B to 99% B) and 30 min (hold 99% B). Data acquisition was controlled by Xcalibur 4.0 and Tune 2.9 software (Thermo Scientific).

The mass spectrometer was operated in data-dependent (dd) positive acquisition mode alternating between a full scan (m/z 380-1580) and subsequent HCD MS/MS of the 10 most intense peaks from full scan (normalized collision energy of 27%). ESI spray voltage was 1.9 kV. Global settings: use lock masses best (m/z 445.12003), lock mass injection Full MS, chrom. Peak width (FWHM) 15 s. Full scan settings: 70 k resolution (m/z 200), AGC target 3e6, maximum injection time 120 Ms. Dd settings: minimum AGC target 8e3, intensity threshold 7.3e4, charge exclusion: unassigned, 1, 8, >8, peptide match preferred, exclude isotopes on, dynamic exclusion 45 s. MS2 settings: microscans 1, resolution 35k (m/z 200), AGC target 2e5, maximum injection time 110 ms, isolation window 2.0 m/z, isolation offset 0.0 m/z, spectrum data type profile.

The raw data was processed using Proteome Discoverer 2.4.0.305 software (Thermo Scientific) and searched against the UniProt database for the Homo sapiens Proteome 2020_01 (74,811 sequences) and the UniProt database for influenza A virus (strain A/Puerto Rico/8/1934 H1N1) 2020_04. The Sequest HT search engine was used to identify tryptic peptides. The ion mass tolerance was 10 ppm for precursor ions and 0.02 Da for fragmented ions. The maximum allowed missing cleavage sites was set to 2. Cysteine carbamidomethylation was defined as constant modification. Methionine oxidation and protein N-terminus acetylation were defined as variable modifications. Peptide confidence was set too high. The processing node Percolator was enabled with the following settings: maximum delta Cn 0.05; decoy database search target FDR 1%, validation based on q-value. Protein label free quantitation was performed with the Minora feature detector node at the processing step. Precursor ions quantification was performing at the processing step with the following parameters: unique plus razor peptides were considered for quantification, precursor abundance was based on intensity, normalization mode was based on total peptide amount, protein ratio calculation was pairwise ratio based, imputation was not performed, hypothesis test was based on t-test (background based). Gene ontology analysis of LC-MS/MS data was performed using Cytoscape (ClueGO app) or STRING online database.

QUANTIFICATION AND STATISTICAL ANALYSIS

Statistical analysis was performed with Graph Pad Prism 9 (GraphPad Software). Quantitative data were attained from at least three independent experiments and represent the means ± standard error mean (SEM). To determine the statistical significance among the experimental groups the two-way ANOVA followed by Dunnett's multiple comparison tests were applied; comparison between two groups were made by Student's t test. All the statistical details of the experiments can be found in the figures' legends. P values of ≤ 0.05 were considered as significant.